Emplacement and high-temperature evolution of gabbros of the 16.5 ºN oceanic core complexes (Mid-Atlantic Ridge): insights into the compositional variability of the lower oceanic crust

Sanfilippo A.[1,2*], Dick H.J.B.[2], Marschall H.R[2,3], Lissenberg C.J.[4] , Urann, B.[2]

1- Dipartimento di Scienze della Terra e dell'Ambiente - Università degli Studi di Pavia, Via Ferrata 1, Pavia, Italy

2-Department of Geology and Geophysics - Woods Hole Oceanographic Institution, Woods Hole, MA 02543, USA

3- Institut für Geowissenschaften, Goethe Universität Frankfurt, Altenhöferallee 1, 60438 Frankfurt am Main, Germany

4- School of Earth and Ocean Sciences, Cardiff University, Park Place, Cardiff CF10 3AT, UK

*Corresponding Author: Alessio Sanfilippo (alessio.sanfilippo@unipv.it)

Key Points:

- Lower crust at the 16.5ºN region of the Mid-Atlantic Ridge has a bimodal composition.
- Thermodynamic models show that this distribution is expected in regions where small gabbroic bodies are intruded into mantle peridotites.
- Deformation related to detachment faulting commenced under high-temperature conditions (>1000 ºC) as recorded by ultramylonites

ABSTRACT

This study reports the composition of the oceanic crust from the 16.5ºN region of the Mid-Atlantic Ridge (MAR), a spreading ridge segment characterized by a complex detachment fault system and three main oceanic core complexes (Southern, Central and Northern OCC). Lithologies recovered from the core complexes include both greenschist facies and weathered pillow basalt, diabase, peridotite and gabbro, while only weathered and fresh pillow basalt was dredged from the rift valley floor. The gabbros are compositionally bimodal, with the magmatic crust in the region formed by scattered intrusions of chemically primitive plutonic rocks (i.e. dunites and troctolites), associated with evolved oxide-bearing gabbros. We use thermodynamic models to infer that this distribution is expected in regions where small gabbroic bodies are intruded into mantle peridotites. The occurrence of ephemeral magma chambers located in the lithospheric mantle enables large proportions of the melt to be erupted after relatively low degrees of fractionation. A large proportion of the dredged gabbros reveal evidence for deformation at high-temperature conditions. In particular, chemical changes in response to deformation and the occurrence of very high-temperature ultramylonites (>1000 ºC) suggest the deformation related to the oceanic detachment commenced at near-solidus conditions. This event was likely associated with the expulsion of interstitial, evolved magmas from the crystal mush, a mechanism that enhanced the formation of disconnected oxide-gabbro seams or layers often associated with crystal-plastic fabrics in the host gabbros. This granulite-grade event was soon followed by hydrothermal alteration revealed by the formation of amphibole-rich veins at high-temperature conditions (~900ºC).

1. INTRODUCTION

Detachment faults, first reported as low-angle normal faults at the MARK area of the MAR (Dick et al., 1981, Karson and Dick, 1983), are common at slow-spreading ridges. These long-lived faults terminate at the foot of the rift valley wall, and produce a smooth surface with corrugations parallel to the rifting direction (Cann et al., 1997). They expose large sections of lower oceanic crust and abyssal mantle, commonly termed "megamullions" or oceanic core complexes (OCCs) (Cann et al., 1997; Tucholke et al., 1998). The detachment faults operate for up to several million years and exhume lower crust and mantle rocks, which are continuously accreted and emplaced into the rift mountains from beneath a volcanic carapace (Dick et al., 2008). Detachment faulting can account for 60–100% of the plate separation in some ridge sections and may dominate a region for several millions of years (Tucholke et al. 1998; Smith et al., 2006, 2008; Schroeder et al., 2007; Baines et al., 2008; Escartín et al., 2008; MacLeod et al., 2009). In particular, Escartín et al. (2008) and Smith et al. (2008) estimated that close to 50 % of the Mid-Atlantic Ridge (MAR) from 12.5ºN and 35ºN is characterized by detachment faults, indicating that a substantial portion of the seafloor in the central portion of the MAR may form by such asymmetric spreading. Recently, some investigators have suggested the proportion of seafloor formed by detachment faulting could be even higher, if more fault surfaces are hidden under basaltic rafted blocks (e.g., Reston and Ranero, 2011). Detachment faulting is now known as a major mechanism of crustal accretion at slow-spreading ridges (Smith et al., 2014; Parnell-Turner et al., 2018).

The nucleation and growth of detachment faults is dependent on many factors, including rheological differences between gabbros and serpentinized mantle peridotites, spreading rate, and magma budget (e.g., Cannat et al., 2006; Ildefonse et al., 2007; Escartin et al., 2008). For instance, numerical modeling suggests that detachment faults form at intermediate levels of magma supply (e.g.: Cannat et al., 2006) at slow- and ultraslow-spreading ridges when the ratio of magmatic accretion to tectonic extension (M) lies between 0.3 and 0.5 (Tucholke et al., 2008; Olive et al., 2010; Hansen et al. 2011). This is consistent with the common occurrence of gabbroic lithologies exposed along the fault surfaces at oceanic core complexes

(e.g.: Dick et al., 1981; 1991; Cann et al., 1997; Dick et al, 2000; Blackman et al., 2007; 2011; MacLeod et al., 2009). In addition, it is likely that the mechanics of detachment faulting in amagmatic environments differs from magmatic ones, where the fault roots into a significant crystal mush zone beneath the rift valley and synmagmatic deformation can enhance fault longevity and control fault geometry (Dick et al., 2000; Natland and Dick, 2001).

OCCs offer a unique opportunity to unravel the composition of the lower crust of ridge segments formed at slow spreading ridges, although these observations are pertinent to the sections exposed through detachment faulting; to what extent these observations apply to the lower oceanic crust at symmetrically-spreading segments is uncertain. The large compositional variability of the gabbros at OCCs worldwide suggests that the lower crust in these sections is not that of the classic Penrose model (Conference Participants, 1972). At the 660-km^2-gabbro massif at Atlantis Bank on the SW Indian Ridge ((I)ODP Holes 735B, 1105A and U1473) most of the gabbros recovered by seafloor sampling and drilling (up to 1.5 km) are olivine-gabbros interspersed with highly evolved (oxide-bearing) gabbros, representing crystallization from nothing close to a primary magmatic liquid (Dick et al., 2000; MacLeod et al., 2017). In contrast, the 1.4 km deep Hole U1309D at the Atlantis Massif OCC, another large OCC exposed along the Mid-Atlantic Ridge, contains a much broader range of lithologies, with large amounts of primitive gabbros such as troctolite, many gabbro sensu-stricto (olivine <5 vol.%) and subordinate oxide-gabbros (>2% oxide) (Blackman 2006, 2010). Large amounts of troctolites and olivine gabbros also constitute the isolated intrusions in mantle peridotites at the Kane Megamullion, a large detachment system south of the Kane Fracture Zone in the Atlantic (Dick et al., 2008), which nonetheless differ from the Atlantis Massif by the absence of olivine-free gabbro but show a high amount of oxide gabbro. Finally, ODP Leg 209 drilled a series of holes from 14°43’ to 15°44’N straddling the 15°20’ Fracture Zone, providing a view of the lithostratigraphy to the south of the 16.5º N core complexes. Notably, gabbro is rare, and the lower crust has a “bimodal” distribution similar to that of the Kane area, with large amounts of troctolite and dunite and

oxide gabbro and oxide gabbronorite the most abundant lithologies. As a whole, the compositional variability of gabbros recovered at OCCs suggests a variable, complex crustal architecture, which emphasizes the need to characterize the lower crust at ridge segments formed at different magma supplies, ridge geometries and tectonics, as part of interpreting crustal petrogenesis.

This study aims at exploring the architecture and the composition of the lower crust exposed along the 16.5ºN region of the MAR. This segment is characterized by a complex detachment fault system developed in a magma-poor regime: unlike the thick gabbroic sections exposed at the Atlantis massif and Atlantis Bank OCCs, oceanic core complexes identified in the 16.5ºN MAR region are formed by scattered gabbroic intrusions within a partly serpentinized mantle (Cannat and Casey, 1995, Cannat et al. 1997. This region is characterized by a strong lateral crustal heterogeneity and an active detachment faulting system (Smith et al., 2014; Parnell-Turner et al. 2016). As such, the MAR 16.5ºN is similar to the Kane and the 15°20' Fracture Zones, and is an ideal case to explore the petrological processes driving the formation of the lower crust in regions of low magma supply and active detachment. Here we present microtextural observations, major element mineral compositions and discuss the process of emplacement and early deformation histories of these rocks. We use thermodynamic modeling to explore the cause of the bimodal lithological variability of the lower crust in this region, proposing that a close relationship between magma supply, eruption rate and deformation-driven melt extraction may explain the lithological variability of the lower oceanic crust exposed through detachment faulting.

2. THE 16.5 ºN REGION OF THE MID-ATLANTIC RIDGE

The study area is located between 16º and 17ºN and exposes an ~120 km stretch of the slow-spreading Mid-Atlantic ridge (Fig. 1). This region encompasses two spreading segments that strike ~012º, perpendicular to the inferred spreading direction (DeMets et al., 2010). The spreading axis is characterized by a well-developed neovolcanic zone and by a remarkably high rate of teleseismic and hydrophone-recorded seismicity (Smith et al., 2003). The area has also been identified as a region of active detachment faulting, mostly concentrated on the west side

of the axis (Escartin et al, 2008).

RV Knorr Cruise 210 Leg 5 conducted bathymetric, dredging and AUV surveys focused on the neovolcanic zone and western rift mountains (see Smith et al., 2014; Parnell-Turner et al., 2018). Based on the occurrence of corrugated surfaces, different core complexes were identified: I) the Southern Core Complex (SCC), a classic, domed, detachment fault with a slope of 13º and corrugation wavelengths between 400 and 1600 m; II); the Central Core Complex (CCC), characterized by two distinctive ridge-parallel, linear ridges (East and West Ridges, Fig. 1), interpreted to be the breakaways of detachment faults that underwent significant rotation (Macleod et al., 2009; Smith et al., 2006; Smith et al., 2008; Parnell-Turner et al. 2018); and III) The Northern Core Complex (NCC). Compared to the South and Central complexes, where the detachment faults intersect the valley floor with a well-developed axial volcanic ridge, the NCC is flanked by a deep axial rift valley, covered by lava flows, but lacking a neovolcanic ridge. This feature suggests that the formation of the NCC was accompanied by limited volcanic activity compared to the Southern Core Complex.

During the RV Knorr Cruise 210 Leg 5 dredging program, we sampled both the footwall of the detachment faults and the volcanic rocks exposed on the associated ridge axis (72 dredges in total). Overall, ~5,800 kg of basalt, diabase, gabbro (s.l.), and peridotite samples were dredged in 63 locations (see Table S1 of the supplementary material). However, the proportions of different rock types vary significantly across the area (Fig. 2). Pillow basalt is the most abundant dredged lithology at all the three core complexes. They have been collected from both the crests of the complexes (i.e. detachment breakaway zone) and as the hanging wall debris resting on the detachment fault footwall. Mantle peridotites (harzburgites to dunites) are abundant in the CCC, whereas only gabbroic rocks were collected at the NCC. A very limited amount of gabbroic lithologies (~1 kg in total) were recovered at the southern and central core complexes, limited to small intrusions within mantle peridotites. The main characteristics of these areas are reported in Smith et al. (2014) and Parnell-Turner et al. (2018). Here we focus our analyses on the NCC and its surrounding areas, capitalizing on the abundance of gabbroic lithologies there to infer lower crustal formation and evolution.

164

165 **2.1. Northern core complex and its surroundings**

166 The gabbros we studied were mainly collected at the Northern Core Complex. This complex is
167 delineated by a detachment fault, which is locally masked by several rafted blocks of volcanic
168 crust. Smith et al. (2014) suggested that these blocks were produced by short-lived steep-
169 dipping normal faults formed close to the rift axis that merged at depth with the primary
170 detachment fault (see Reston and Ranero, 2011). Each fault block is covered by volcanic
171 hummocks and flows similar to those on the valley floor. The median valley adjacent to the
172 NCC is narrow (3–4 km) and deep (~4,500 m), and is characterized by smooth, likely
173 sedimented surfaces covering flat-topped lava flows and hummocks. Although there is no
174 neovolcanic axial ridge, the occurrence of volcanic ridges and hummocks emerging from the
175 sediments at the west side of the median valley and the flows on the rift valley floor suggest
176 that this segment was volcanically active in the recent past. Several dredges were deployed at
177 the central portion of the NCC, recovered 579 kg of fresh pillow basalts from the terrace of the
178 rafted block (D52, D56, D57, D65).

179 237 kg of gabbroic rocks were recovered in 10 of 14 dredge hauls (i.e., D49 to D55, D59,
180 D60, D63, D64, D67, D69, D70, D72) deployed along a ridge around the complex (from the
181 southern shoulder to two narrow ridges in the north). Gabbros in this locations are associated
182 with 157 kg of peridotite sampled in 8 dredges and 513 kg of fresh pillow basalts found in 6
183 dredges. Dredged gabbros were described macroscopically during the expedition. Each
184 member of the Shipboard Party was responsible for one or more aspects of the description (e.g.,
185 rock-type, textures, mineral modes and habits) to ensure consistency throughout the dredged
186 hauls. Only primary minerals were considered to define the initial modal proportion;
187 completely altered rocks are referred to as metagabbros (Table S1 of supplementary material).
188 Representative sample images are displayed in Figure 3. Preliminary onshore analyses followed
189 the shipboard observations in order to test the accuracy of the definition of rock types and
190 deformation intensity. Samples reviewed for the present study provided a good correspondence
191 with the shipboard observation, although minor interstitial phases such as orthopyroxene and

amphibole had been commonly underestimated (see textural description). This generally did not affect the classification of the rock types, which is based on major mineral phases. The proportions (wt.%) of different gabbroic rocks collected from each dredge are reported in Figure 2, which shows that the lower crust exposed at NCC displays a bimodal distribution, i.e., high proportions of primitive plutonic rocks (i.e., dunites and troctolites >60 wt.%) associated with evolved gabbronorites to oxide gabbros (~30 wt.%). Intermediate rocks such as olivine gabbros (olivine >5 vol.%; clinopyroxene >10 vol.%; oxides <2 vol.%) and gabbros *sensu strictu* (olivine <5 vol.%; oxides <2 vol.%) and gabbronorite (olivine< 5vol.%; orthopyroxene >5 vol.%) are very limited, as they are to the south. Interestingly, troctolites were mainly collected in two dredges (D59, D60; Fig. 2) otherwise characterized by large proportions of serpentinized dunites and pyroxene-bearing peridotites, and by the absence of volcanics. The exposure of mantle peridotites, dunites and troctolites and rarity of basalts are typical of sequences thought to represent crust-mantle transitions, such as the OPD Site 895 at Hess Deep (Dick and Natland, 1996), the Adam Dome at the Kane FZ (Dick et al., 2008), the breakaway area of the Godzilla Megamullion (Sanfilippo et al, 2013; 2016a), and the Uraniwa Hills at the Central Indian Ridge (Sanfilippo et al., 2015; 2016b).

3. MAIN PETROGRAPHIC FEATURES OF MAR 16.5º N GABBROS

3.1 Igneous textures

Troctolites have euhedral to subhedral olivine and plagioclase, locally showing sub-rounded grain boundaries and a poikilitic texture (Fig. 4a). Clinopyroxene commonly occurs as films or discrete grains interstitial to olivine and plagioclase. Large clinopyroxene oikocrysts (up to 7 mm) are locally present within the olivine-plagioclase matrix, commonly including euhedral to irregular plagioclase and olivine chadacrysts (Fig. 4b). Clinopyroxene oikocrysts show film-like apophyses interstitial to olivine and plagioclase, locally associated with orthopyroxene films. In a few cases, oikocrystic clinopyroxene reaches 10 vol.% of the rock, forming spatially defined Ol-gabbro domains. Pargasitic brown amphibole is common within the troctolites as films or interstitial discrete grains locally reaching 0.1 mm (Fig. 4c). One

troctolite contains large amphibole oikocrysts up to 3 mm. These oikocrysts include rounded plagioclase chadacrysts, having irregular grain boundaries taken as evidence of partial dissolution (Fig. 4d). Fe-Ti oxides are locally present in troctolites, but are restricted to within the interstitial brown amphibole at the rim of olivine or plagioclase.

Gabbros and gabbronorites consist of plagioclase and pyroxenes commonly showing a subophitic texture. Olivine is absent or restricted to small grains (<0.5 mm) rounded in shape. Small (<0.1 mm) irregular grains of Ti-Fe oxides and apatite are locally included in the pyroxenes or at the rim of pyroxene-plagioclase crystals. Orthopyroxene in gabbronorites occurs in large, subequant crystals with subhedral habit, as distinguished from intergranular rims commonly found in olivine gabbros. Pargasitic brown amphibole is rare in these rocks, and present as <0.05 mm-thick films around clinopyroxene.

Oxide gabbros (>2% oxide) have been found as i) coarse (up to 20 cm) grained massive samples and as ii) medium/fine-grained centimeter-sized seams crosscutting either gabbros or gabbronorites. In both cases, oxide gabbros are mostly constituted by granular plagioclase, clinopyroxene and locally orthopyroxene, and abundant (up to 15 vol.%) Ti-Fe oxides. Olivine is absent from all of these rocks, whereas accessory phases such as zircon and apatite are commonly present. Brown pargasitic amphibole is ubiquitous within the oxide gabbros, occurring as interstitial grains to coronas surrounding opaque minerals or as blebs within partly exsolved clinopyroxene. Coarse-grained oxide gabbros contain irregular oxide-rich patches up to 10 mm wide separating, and in some cases, surrounding aggregates of disrupted plagioclase and clinopyroxene grains. The oxide-rich domains locally include small plagioclase and/or apatite grains (0.1-0.5 mm), subhedral to rounded in shape. The oxide-gabbro seams are typically found as medium to fine-grained, centimeter-sized layers parallel to the foliation in the host rock. They have a planar aspect and well-defined sutured contacts with the host gabbros, although oxide minerals can be locally dispersed in the host rock a few millimeters from the contact.

3.2 Textures indicative of high-temperature deformation

Metamorphic grade and crystal-plastic fabric intensity were documented for each sample, which were cut perpendicular to the foliation where possible. Approximately 40% of the gabbros preserve textures indicative of shearing and recrystallization under hyper- to subsolidus conditions. Deformation intensity was classified on a scale from 0 to 5 (0, undeformed; 1, slightly deformed; 2, sheared; 3, protomylonitic; 4, mylonitic and 5, ultramylonitic) based on the foliation, grain size and relative proportions of neoblasts and porphyroclasts. The distribution of the deformation intensity for the different rock-types (Fig. 5) suggests that the higher grade crystal-plastic deformation (grades 3 to 5) is equally recorded by primitive and evolved gabbros, while oxide gabbros and gabbronorites seem to be on average more deformed than troctolites (~50% and ~30% of the total, respectively) at lower grades.

3.2.1-Granulite grade deformation

Protomylonites and mylonites generally appear to be indistinguishable on the basis of mineral proportions from their protoliths, which is not the case for ultramylonites (Fig. 6a; b). Protomylonites are defined by the occurrence of a porphyroclastic texture that locally grades into mylonites having alternating bands of neoblastic plagioclase, olivine and/or clinopyroxene (Fig. 3). The mylonitic zones are up to decimeter wide, although we cannot determinate the original thickness because undeformed portions of the same rock are not recovered. The most common metamorphic assemblage includes recrystallized olivine, pyroxenes and plagioclase. Depending on the protolith, spinel (in troctolites) or Ti-Fe oxides (in gabbros and oxide gabbros) are also found as neoblastic phases. Olivine, pyroxenes and plagioclase porphyroclasts are kinked, folded, and displaced by subgrain boundaries. Equant to subequant neoblasts surround porphyroclasts of the same mineral, suggesting subgrain boundary rotation and recrystallization under high-temperature conditions (Miranda and John, 2010; Hansen et al., 2013). Trace amounts of pargasitic amphibole are locally found within the neoblastic assemblage, as small (<0.1 mm) grains in textural equilibrium with the major phases. Samples showing this metamorphic assemblage will be referred to hereafter as

"gabbro granulites", in analogy with the definition of similar rocks from other oceanic core complexes worldwide (see Dick et al., 2000; Blackman et al., 2006; 2011; Ildefonse et al., 2007; Dick et al., 2008; Miranda and John, 2010; Hansen et al., 2013; MacLeod et al., 2017).

3.2.2-Ultramylonites

The mylonites locally grade into 5 to 10-mm thick, very fine-grained (<0.1 mm) ultramylonitic bands. These bands are always found in the median portions of the mylonites, and have sub-planar shape and sharp boundaries towards the host rock (Fig. 3). Unlike the mylonites, which are mineralogically indistinguishable from the magmatic protolith, the ultramylonites have a distinct mineralogical composition. We found ultramylonites developed from different protoliths ranging from troctolites (Fig. 6a) to oxide gabbros (Fig. 6b). These two end-members will be described hereafter.

i) Figure 6a shows a ~5-mm thick ultramylonite located within a troctolite mylonite. The host protomylonite and the mylonite are formed by olivine and plagioclase porphyroclasts mantled by a neoblastic assemblage of plagioclase and olivine, locally including clinopyroxene and brown amphibole (Ti-pargasite). Spinel porphyroclasts are also present and partly recrystallized along the main foliation planes. In contrast, olivine and spinel are absent in the ultramylonite band, which is mainly formed by a very fine-grained (<0.1 mm) assemblage of plagioclase and brown amphibole (Ti-pargasite) and rare clinopyroxene. Both clinopyroxene and brown amphibole are locally replaced by green amphibole and chlorite in a coronitic texture.

ii) Figure 6b shows an up to ~5-mm thick ultramylonite band located within an oxide-gabbro mylonite. The host mylonite is characterized by plagioclase and clinopyroxene porphyroclasts immersed in a neoblastic assemblage of plagioclase, clinopyroxene and Ti-Fe oxides (~5-10 vol.%). Pale to green amphibole (hornblende) statically replacing the neoblastic clinopyroxene is abundant, whereas brown amphibole is absent. In contrast, the ultramylonite band is characterized by a very fine-grained assemblage of plagioclase and brown amphibole (Ti-pargasite) locally associated with minor clinopyroxene, and by the absence Ti-Fe oxides. Similar to the ultramlylonite located in the troctolite, green

amphibole and chlorite locally replace the brown amphibole and the clinopyroxene. Taken as a whole, despite the fact that the two ultramylonites developed from different magmatic protoliths, the ultramylonites are texturally and mineralogically indistinguishable, consisting of a fine-grained neoblastic assemblage of plagioclase, brown amphibole and, more rarely, clinopyroxene.

3.3 Textures indicative of high-temperature alteration

Deformed gabbros locally show traces of alteration at high-temperature conditions (amphibolite facies). This process is mainly indicated by *i)* the occurrence of amphibole-rich veins crosscutting the foliation in the host gabbros at high angle; *ii)* the occurrence of pale-brown amphibole (hornblende) statically replacing the clinopyroxene. These textures are well exemplified in Figure ~~3e~~3f, which shows a sheared gabbronorite crosscut by an undeformed amphibole-rich vein, at high angle with the main foliation in the host rock. Hornblende in the veins shows a fibrous texture and is elongated parallel to the vein wall. Plagioclase close to the contact with the vein is statically recrystallized in a fine-grained assemblage. Clinopyroxene in the host gabbro is almost totally replaced by single grains or aggregates of hornblende spatially locally associated with very fine-grained (<0.05 mm) albitic plagioclase (Fig. 3f). Similar textures are also found where irregular veins crosscut the gabbros, leading to the formation of hornblende at the expense of clinopyroxene, and fine-grained plagioclase replacing the coarse plagioclase of magmatic origin. In almost all of the samples, hornblende is locally rimmed or partially replaced by green amphibole and chlorite, as a response to lower-temperature greenschist facies alteration.

4. MAJOR ELEMENT MINERAL COMPOSITIONS

Major element mineral compositions of selected 16.5ºN gabbros were obtained using a JEOL JXA-8200 electron microprobe (Dipartimento di Scienze della Terra, Universita`degli Studi di Milano, Italy) at 15 kV accelerating voltage and 15 nA beam current. Counting time was 30 s on the peak and 10 s on the backgrounds. Natural silicates were utilized as standards and data

reduction was carried out using the CITZAF package (Armstrong 1995). Undeformed and variably deformed samples ranging from troctolites to oxide gabbros were selected for the microprobe study, in order to cover the main chemical variability of the rock-types. Representative analyses of olivine, plagioclase, pyroxene and amphibole of selected samples are reported in supplementary material in Tables S2 to S6. Four samples were also mapped using a Zeiss Sigma HD field emission gun SEM installed at Cardiff University. This machine is equipped with dual 150-mm^2 Oxford Instruments X-Max^N energy dispersive silicon drift detectors, which enable high count rates (>1,000,000 cps) to be obtained. The data were background corrected using Oxford Instruments AZtec software prior to the production of element maps.

Olivine in troctolites has high forsterite (Fo) contents (86 to 88 mol.%), and relatively constant NiO (0.20–0.25 wt.%) and MnO (0.19–0.25 wt.%) contents. There is no compositional difference between porphyroclastic and neoblastic olivine. Plagioclase anorthite content varies from An_{81} in troctolites to An_{46} in oxide gabbros. Chemical analyses and element maps clearly show that high-temperature deformation is associated with a decrease in anorthite in plagioclase neoblasts compared to porphyroclasts in the same rock. This is well illustrated in Figure 7a, where compositional maps for Na contents of a sheared troctolite are shown. In particular, the lower Na (and higher Ca, not shown) of the fine-grained neoblasts clearly indicates lower An contents (~78 mol.%) compared to that of the porphyroclasts (~81 mol.%). Similarly, an even greater variation in plagioclase anorthite component characterizes the troctolite mylonite–ultramylonite association (Fig. 7b). Here, the plagioclase in the ultramylonite has lower Ca (and higher Na) compared to that in the mylonite, resulting in a decrease from An_{81} in the mylonites to An_{65} in the ultramylonite. A unique exception is represented by the mylonite–ultramylonite association in the oxide gabbronorite (Fig. 7c), where compositional maps show higher Ca and lower Na contents of the plagioclase in the ultramylonite (An_{82}) compared to that in the host mylonite (46 mol.%). Finally, a decrease in anorthite component is apparent in recrystallized plagioclase associated with the formation of the amphibole-rich vein in Figure 7d. Here, the neoblastic plagioclase at the Amphibole-

359 vein/gabbro contact and the plagioclase in the vein has higher Na and lower Ca compared to the
360 plagioclase porphyroclasts, resulting in An_{53} for the former and ~An_{58} for the latter. Note that
361 very high Na and low Ca characterize the fine-grained plagioclase associated with veins and
362 microcracks crosscutting the magmatic phases (An_{20} to An_{25}).

363 Clinopyroxene shows a wide compositional range with Mg# (100*Mg/{Mg+Fe})
364 varying from 89 in oikocrystic clinopyroxene in troctolites to 65 in oxide gabbros.
365 Clinopyroxene in troctolites is distinct from that in gabbros by generally higher Cr_2O_3 and
366 Al_2O_3 contents (0.4–1.5 wt.% compared to <0.2 wt.% in the gabbros), but high TiO_2 contents
367 (Fig. 8). Chemical mapping suggests that clinopyroxene neoblasts in sheared to mylonitic
368 rocks are nearly indistinguishable from the porphyroclasts in the same sample. The only
369 exception is the clinopyroxene in oxide gabbro mylonites/ultramylonite shown in Figure 7c,
370 which has a sharp change in chemical composition from the mylonite (Mg#=64–67;
371 Cr_2O_3=0.01–0.02 wt.%) to the ultramylonite (Mg#=73; Cr_2O_3=0.5 wt.%). With the exception
372 of this ultramylonite, there is a positive correlation between Mg# in clinopyroxene and
373 anorthite content in coexisting plagioclase from each sample (Fig. 9a).

374 Orthopyroxene Mg# is well correlated with Mg# of coexisting clinopyroxene (Fig. 9b).
375 Similar to clinopyroxene, orthopyroxene from our sample suite is characterized by (*i)* high Mg#
376 and Cr_2O_3 contents (87–89; 0.4–0.6 wt.%, respectively) in troctolites and progressively lower
377 (75–58; 0.01–0.04 wt.%) in gabbro/gabbronorite/oxide gabbro, and (*ii)* lack of correlation
378 between TiO_2 and Mg#. The composition of the coronitic to interstitial orthopyroxene in the
379 troctolites suggest a magmatic rather than a metamorphic origin, similar to the granular
380 orthopyroxene in the gabbronorites.

381 Amphibole is a ubiquitous phase in our samples. There is a clear chemical distinction
382 between the green to pale-brown amphibole statically replacing clinopyroxene (Type I) and the
383 brown amphibole forming poikilitic to interstitial grains in undeformed samples or found as
384 neoblasts within the granulites (Type II; Fig. 10). Type I amphibole occurs in two forms: i)
385 green amphibole with very low Al^{IV} (<0.39 atoms per formula unit, apfu), TiO_2 (<0.41 wt.%)
386 and alkalis [(K+Na)<0.12 atoms per formula unit, apfu], mainly consisting in actinolite and

tremolite (Fig. 10); ii) pale-brown amphibole, having higher Al^{IV} (0.83–1.29 apfu), TiO_2 (0.3–1.4 wt.%) and alkalis (0.49–0.78 apfu) and mostly represented by hornblende (Fig. 10b). Pale-brown hornblende also constitutes the amphibole-rich veins. These amphiboles have Al^{IV} (1.24–1.41 apfu) and alkalis (0.51–0.82 apfu) partly overlapping those in the amphibole coronas, but have higher TiO_2 contents (3.0–3.3 wt.%). TiO_2 contents of the hornblende in the vein decrease towards the rim. Chlorine in hornblende coronas and hornblende in veins varies between 0.1–0.2 wt.% (Fig. 10b, c).

In contrast, Type II amphibole is brown to reddish brown, and mostly consists of Ti-pargasite. Within the undeformed troctolite and gabbro samples, this amphibole has high Al^{IV} (1.74–1.82 apfu) and alkalis (0.61–0.79 apfu) and very high TiO_2 contents (4.2–4.9 wt.%) and high Mg# (Fig 10d). Chlorine is lower than the detection limit of the microprobe analyses (~ 0.1 wt.%) (Fig. 10b, c). Similar to the hornblende in the amphibole veins crosscutting the gabbros, the large amphibole oikocryst in troctolites show a sharp decrease in Al^{IV} and TiO_2 from the core towards the rim. Amphibole neoblasts in mylonites and ultramylonites are chemically similar to the magmatic amphibole in undeformed samples. They have high Al^{IV} (1.50–1.82 apfu) and alkalis (0.62–1.80 apfu), low chlorine (<0.1 wt.%), and highly variable TiO_2 contents (1.5 to 4 wt.%). The neoblastic amphiboles in the two ultramylonites are overall similar to both the magmatic amphibole and the neoblastic amphibole in the mylonite. The amphibole in the troctolitic ultramylonite tends to have higher Al^{IV} and TiO_2 contents and Mg# than the amphibole in the oxide gabbro ultramylonite (Fig. 10b; d).

5. DISCUSSION

5.1-Bimodal distribution of gabbros from the 16.5º N region of Mid-Atlantic Ridge: a quantitative model to explain the compositional variability of the lower oceanic crust

The composition of the gabbroic rocks collected from the 16.5º N region of the MAR indicates a lower oceanic crust most likely formed by scattered intrusions of chemically primitive gabbros (i.e. troctolites), mainly associated with evolved gabbronorites and oxide-rich gabbros. Intermediate rocks such as olivine-gabbros and gabbro *sensu stricto* are restricted to <3 wt.% of the ~356 kg of gabbros sampled in the region (Fig. 2). This bimodal distribution is

415 remarkably different to that of the gabbroic section drilled at Hole U1309D (Blackman et al.,
416 2006; 2011), formed in a relatively robust magmatic center along the Mid-Atlantic Ridge
417 (Godard et al., 2009). It also contrasts sharply with the Atlantis Bank gabbro massif on the SW
418 Indian Ridge, which is dominated by moderately fractionated olivine gabbro that grades into
419 subordinate highly evolved oxide gabbros (e.g.: Dick et al., 2000; MacLeod et al., 2017).
420 Motivated by the similarity of the gabbros exposed in the 16.5ºN region with those of the Kane
421 Megamullion and in the vicinity of the 15°20'Fracture Zone, hereafter we examine how magma
422 supply and melt extraction may control the overall composition of the crustal sections exposed
423 through detachment faulting. We calculate the relative amount of different gabbroic lithologies
424 (i.e. dunites, troctolites, olivine gabbros, gabbros and oxide gabbros) crystallized during a
425 fractional crystallization process using the thermodynamic program *MELTS* (Ghiorso and
426 Sacks, 1998; Ghiorso et al., 2002). In order to take into account that part of the initial liquid
427 mass is erupted as basalt on the seafloor, we performed this calculation in different steps,
428 allowing a proportion of the liquid to be subtracted at each step of the crystallization process
429 (parameters and results of the model in Tables S7, S8, S9 of the supplementary files). The
430 starting liquid (*Liq 0*) is a primary melt formed by ~10 % melting of a DMM peridotite source
431 (Mg# ~72; Kinzler and Grove, 1993). After a defined amount of differentiation (for the sake of
432 simplicity fixed at ΔMg# ~4), a precise mass of liquid *(Liq 1)* is subtracted and the remaining
433 composition of *Liq 1* is used as initial composition for the next step of differentiation. The
434 mass of liquid subtracted is calculated by scaling the melt mass in proportion to the
435 compositional distribution of the erupted basalts, which is thereby a fundamental input of our
436 model. We cannot use the observed compositional variability of basalts sampled exclusively in
437 the 16.5ºN region, considering that the genetic relationships between the basalts along axis and
438 the gabbros exposed through detachment faulting is not obvious and that basalt sampling is
439 inevitably fragmentary. It has been previously noted that the compositional distribution of
440 basalts at the MOR is globally dependent on the spreading rates (Melson et al., 1976; Sinton
441 and Detrick, 1992). In particular, basalts erupted at slower-spreading ridges tend to be more
442 primitive compared to those erupted at fast-spreading ridges (Fig. 11). The large-scale

443 compositional variability of the basalts can thereby be considered meaningful, and allows us to
444 compare the results of our model with different lower crustal sections exposed along the same
445 ridge segment. Here, we used the overall compositional distribution of the basalts erupted along
446 the 10–35ºN segment of the MAR, which comprises ~2,700 glass analyses selected from the
447 PetDB database (reference Lehnert paper), making the necessary assumption that the
448 distribution is constant for all the modeled scenarios. An explanation of the model is reported in
449 Figure 12.

450 The solid composition is calculated at each step from the total mass of crystallizing
451 phases given by the program (Fig. 13a; b). The crystallizing phases are restricted to olivine,
452 plagioclase, clinopyroxene and Fe-Ti oxide, following the fractionation trends inferred for a
453 MORB melt (see Grove et al., 1993). Minor phases such as orthopyroxene and amphibole are
454 not considered in the model because they occur as interstitial phases, likely related to
455 crystallization from intercumulus melt. This is in contrast to the primitive orthopyroxene-
456 bearing cumulates that have been sampled in different locations along the mid-ocean ridge
457 system. The orthopyroxene from these rocks has primitive compositions and may represent
458 crystallization from melts more depleted that typical MORB (e.g., Ross and Elthon 1995) either
459 derived from melting an hydrated mantle (Nonnotte et al. 2005) or from melt residual by
460 interaction with mantle peridotites (see also discussion in Gillis et al. 2014). However, it should
461 be noted that gabbronorites having granular orthopyroxene as a cumulus phase were rarely
462 sampled in this study, and that these rocks do not contain olivine and have relatively evolved
463 mineral compositions, plotting in the field of the orthopyroxene-free gabbros (Figs 8 and 9).
464 For the sake of simplicity, we hence grouped the gabbronorites with the gabbros *sensu stricto*
465 in our model. The total mass of initial liquid subtracted by eruption (M_e) with respect to that
466 crystallized (M_c) is referred to as M_e/M_c. At M_e/M_c =0 the melt is totally retained in the lower
467 crust and the mass of gabbro crystallized corresponds to that of pure fractional crystallization.
468 At high Me/Mc the melt is preferentially erupted and the relative mass of crystallized gabbros
469 decreases.

470 The proportion (mass %) of gabbros crystallized at different M_e/M_c (0 to ~7:3) is

shown in Figure 13, where the chemical and modal compositions of the crystallizing assemblages and the distribution of the resulting erupted basalts are shown at steps of ΔMg# 4. Remarkably, the olivine and clinopyroxene crystallized from the computed melt fits the composition of the natural samples from this study very well. As was expected, this model shows that at increasing M_e/M_c, a large proportion of the melt is erupted on the seafloor during the first phase of crystallization. Hence, the crystallizing assemblage tends to be progressively more primitive, i.e.: olivine ± plagioclase assemblages are preferentially formed until the melt is exhausted (Fig. 13e). At the same time, at high M_e/M_c ratios most of erupted melts are restricted to basalts with very primitive compositions.

This simple scenario is highly improbable, however, as it implies that the liquid mass is entirely extracted from the cumulate at each step of differentiation. Studies of oceanic gabbros indicate that variable amounts of interstitial melt are retained within the crystal mush (e.g.: Meyer et al., 1989; Natland and Dick, 2001). Hence, we assume that a proportion of the initial melt is retained at each step of the crystallization process, following a separate liquid line of descent (see Fig. 12). We must consider that the interstitial melts can crystallize within the cumulus matrix at the closure of the magmatic system (e.g.: Tribuzio et al., 2000; Borghini and Rampone, 2007) or can migrate through the crystal mush driven by buoyancy differences or by compaction (e.g.: Dick et al., 2000; Natland and Dick, 2001). In both cases, textural and geochemical evidence in gabbros suggest that these melts tend to partly assimilate the crystal matrix, causing geochemical modification ascribable to assimilation–fractional-crystallization (AFC) processes (e.g.: Coogan et al., 2000; Borghini and Rampone, 2007; Gao et al., 2007; Lissenberg and Dick, 2008; Drouin et al., 2009; Sanfilippo et al., 2013; Lissenberg and MacLeod, 2016). The chemical response to these processes has been modelled following equations from DePaolo (1981). These equations replicate the variations in trace element compositions of the reacting melts and of the phases crystallized from it (see Coogan et al., 2000; Gao et al., 2007; Borghini and Rampone, 2007; Lissenberg et al., 2013; Sanfilippo et al., 2015; Lissenberg and MacLeod, 2016). They have been successfully used to test AFC hypotheses in well-constrained melt-rock reaction scenarios, such as the conversion

499 of dunite to troctolite (e.g., Rampone et al., 2016 and reference therein) or troctolite to
500 olivine-gabbro (Lissenberg and Dick, 2008). When applied to the scale of the entire oceanic
501 crust, a process of assimilation would introduce a number of independent variables (i.e., the
502 modal amount of mineral phases involved; the chemical compositions of the reactants; the
503 mass assimilate/mass crystallized ratios; see discussion in Lissenberg et al., 2013). Such a
504 model could not be reproduced by the *MELT* model used here.

505 As a simplification, at each step we subtracted a certain amount of melt proportional
506 to the melt density (Fig. 13d), considering that a maximum of 30% of liquid can initially be
507 trapped in the solid framework before migrating upwards due to compaction by density
508 driven flow (Morse, 1979; Meyer et al., 1989). Then we calculate the gabbros crystallized
509 from the total mass of trapped melts (Fig. 12). The mass of gabbro resulting from this
510 calculation was then added to that of the gabbros previously obtained. Note that owing to an
511 increase in melt density with the chemical evolution, our model supposes that the amount of
512 melt potentially trapped in the crystal framework increases at decreasing liquid Mg#. This
513 causes a dependence of the amount of trapped melt on the M_e/M_c ratio, with a more extensive
514 melt entrapment occurring at low M_e/M_c ratios (Fig. 13e).

515 As expected, this calculation shows that the relative amount of evolved lithologies
516 (mainly oxide-gabbro) increases in all the modelled scenarios (Fig. 13e). In particular, at high
517 M_e/M_c ratios, most of the initial liquid is erupted on the seafloor before the melts reach
518 saturation in clinopyroxene, thereby preventing the formation of moderately evolved gabbros
519 (olivine-gabbros and gabbros *sensu stricto*). However, at the same time, the occurrence of
520 trapped liquid enables the local formation of evolved lithologies as this melt migrates due to
521 upward compaction and lateral density driven flow (gabbronorites to oxide gabbros). As a
522 consequence, at high *Me/Mc* ratios the model is able to produce a bimodal distribution of the
523 gabbros, characterized by large proportions of primitive lithologies and lack of intermediate
524 compositions.

525 It is noteworthy, however, that the model fails to reproduce the large amount of oxide
526 gabbros present in the 16.5 ºN region. There are several factors that can account for this. Most

527 oxide gabbros appear to be formed by interstitial melts expelled from the cumulate matrix and
528 by upward compaction and/or high temperature deformation into narrow zones of the crystal
529 mush often associated with shear zones along the detachment fault surface (Dick et al., 2000;
530 Natland and Dick, 2001; Macleod et al., 2017). Moreover, it has been recently observed that in
531 addition to an upward increase in oxide gabbros at the Atlantis Bank gabbro massif, that the
532 body is laterally zoned to more evolved cumulates that comprise the entire section from the
533 base of the crust to the dike-gabbro transition at the distal end of the body near the bounding
534 Atlantis II Transform (MacLeod et al., 2017). This shows that density driven lateral flow by
535 either direct intrusion or permeable flow plays a major role in the architecture of the lower
536 oceanic crust. Thus, as seen at the Kane Megamullion (Dick et al., 2008) and Atlantis Bank
537 (MacLeod et al., 2017), while dunite and troctolitic dikes are rare in mantle massifs adjacent to
538 major magmatic centers at slow spreading ridges, oxide gabbro dikes are widely distributed
539 lithology. Thus, the amount of oxide gabbros can be biased by dredging and drilling in areas of
540 low magma flux, with highly centralized magmatic centers and intervening relatively
541 amagmatic regions, as from 13° to 17°N on the MAR (e.g.: Mendel et al., 1997, Sauter et al.,
542 2001, Standish et al., 2008). Finally, we emphasize that any AFC process would tend to
543 increase the incompatible element composition of the interstitial melt (see Lissenberg and
544 MacLeod, 2016 and reference therein), producing melts anomalously enriched in incompatible
545 elements compared to a melt evolving through fractional crystallization. This suggests that a
546 melt produced by AFC would potentially enriched the melt in Ti, bringing the saturation in Fe-
547 Ti oxides forward, and producing higher amounts of oxide-bearing lithologies. This is another
548 possible reason why our model seems to underestimate the amount of oxide-gabbros compared
549 to the natural occurrences.

550 Although fairly simplistic, in combination with insight provided by field mapping into
551 ocean crust architecture, this model provides insight into why a bimodal distribution of the
552 lower oceanic crust may be expected in regions where a high proportion of liquid produced in
553 the mantle is erupted on the seafloor, with a minor proportion of intrusive rocks. This scenario
554 recalls the “plum-pudding model” suggested for slow-spreading ridges (Cannat, 1993, Cannat

et al., 1995; 1997), which proposes that the lower oceanic crust might consist of small gabbroic plutons scattered within the lithospheric mantle (see also Kelemen et al., 2004; Dick et al. 2008; 2010).

The outcomes of our model are consistent with the compositional heterogeneity of the lower oceanic crust along the MAR (Fig. 13). For instance, a lower oceanic crust mainly consisting of primitive gabbros and highly evolved lithologies is expected at regions characterized by scattered injections intruded within mantle peridotites, such as the region considered here or the 15º20'N fracture zone drilled during Leg 209 (Kelemen et al., 2004). On the other hand, a lower oceanic crust mostly composed of moderately evolved gabbros associated with primitive lithologies (troctolites and dunites) and minor oxide gabbro is expected in areas of a thick crust and moderate melt supply. This can be the case for relatively robust magmatic segments as for instance the Atlantis Massif OCC (Blackman et al., 2007; 2011; Ildefonse et al., 2007; Godard et al., 2009; Drouin et al., 2009; 2010) or the crustal transect exposed at the Adam Dome of the Kane megamullion (Dick et al., 2008) (Fig. 12d).

5.2 Emplacement and crystal-plastic deformation of the NCC gabbros

Clinopyroxene in the 16°30'N gabbros are characterized by different combinations of Mg# and TiO_2 contents (Fig. 8). In particular, they show two distinct chemical trends in troctolites (Trend 1) and gabbros/gabbronorites/oxide gabbros (Trend 2). The clinopyroxenes following Trend 1 show a sharp increase in TiO_2 at nearly constant Mg#; whereas those following Trend 2 display a gradual increase in TiO_2 at decreasing Mg# followed by (from Mg# ~70) a renewed decrease in TiO_2. These chemical trends are typical for clinopyroxene from abyssal gabbros (see Coogan, 2007) and respectively explained as (Trend 1) evidence for magmatic metasomatism (i.e., melt–rock reactions) in a troctolitic matrix (see also Lissenberg and Dick, 2008; Suhr et al., 2008; Drouin et al., 2009; Sanfilippo and Tribuzio, 2013; Sanfilippo et al., 2013; 2015a; b; Lissenberg and MacLeod, 2016); (Trend 2) evidence for progressive magmatic differentiation followed by saturation in Fe-Ti oxides to form the oxide gabbros. The gradual decrease in clinopyroxene Mg# versus

583 plagioclase An contents, and the variability of the Cpx suggest that the
584 troctolite/gabbro/oxide-gabbro series crystallized from cogenetic melts evolving through
585 fractionation of Ol, Pl, Cpx and, finally, Ti-Fe oxides. Despite this, it seems obvious that the
586 crystallization of Cpx in the troctolites also involved interactions between the olivine and
587 plagioclase matrix and an evolved interstitial melts. This is consistent with the occurrence of
588 large brown amphibole occurring as interstitial to oikocrystic grains within the troctolites
589 (Fig. 4c;d). This amphibole locally shows poikilitic textures with inclusions of irregular
590 plagioclase chadacryst and small Ti-Fe oxides, and is characterized by high TiO_2, (K+Na)
591 and Al, and negligible Cl contents (Fig. 10). The poikilitic texture and the chemical
592 compositions are reconcilable with a magmatic origin, indicating the crystallization of late-
593 stage melts enriched in water and incompatible elements (see also Tribuzio et al., 2000;
594 Coogan et al., 2001; Borghini and Rampone, 2007). Hence, in agreement with the extensive
595 literature data for abyssal gabbros (e.g., Lissenberg et al., 2008; Suhr et al., 2008; Drouin et
596 al., 2009; Renna and Tribuzio, 2010; Sanfilippo et al., 2013; 2015; Lissenberg and MacLeod,
597 2016; Rampone et al., 2016), the enrichments in TiO_2 in the high-Mg# clinopyroxene and the
598 occurrence of magmatic amphibole with poikilitic texture testify that the 16.5ºN troctolites
599 underwent a process of magmatic metasomatism by an interstitial, evolved melt. Below, we
600 show that evolved melts were also locally present at the onset of the deformation related to
601 the detachment faulting.

602 A large proportion of the 16.5ºN gabbros show textures associated with a process of
603 deformation under high-temperature conditions (Fig. 3). In particular, most samples have
604 olivine, plagioclase, and clinopyroxene recrystallized in polygonal aggregates that are often
605 associated with brown amphibole and Ti-Fe oxides. The amphibole neoblasts in all deformed
606 troctolites (sheared, mylonites, and ultramylonites) are compositionally identical to the
607 magmatic amphibole in the undeformed samples. In addition, the occurrence of deformed
608 amphibole porphyroclasts in a sheared troctolite and the textural equilibrium with the other
609 neoblastic phases (olivine, plagioclase and clinopyroxene) clearly indicate that the formation
610 of pargasitic amphibole in this sample predated the “anhydrous” granulite-facies deformation

611 event.

612 The edenite-richterite amphibole-plagioclase thermometer of Holland and Blundy
613 (1994) on adjacent grains of amphibole and plagioclase was selected to infer the temperature
614 of recrystallization (Fig. 14). In one mylonitic troctolite, the amphibole-plagioclase
615 thermometry was also confirmed by two-pyroxene thermometry (Lindsley and Frost, 1992),
616 which yielded similar temperature estimates (see Fig. 14). Independent of rock-type, the
617 amphibole-plagioclase thermometer provided high temperature estimates for the granulite-
618 grade deformation, varying between 930 ºC and ~1010 ºC. These estimates fall in the range
619 of temperature estimated by Mehl and Hirth (2008), who showed that granulite-facies
620 deformation in gabbros from Hole 735B occurred at temperatures as high as 946 ±70 ºC.
621 These data suggest that the crystal-plastic deformation, which caused dynamic
622 recrystallization and formation of neoblasts of olivine + clinopyroxene ± brown amphibole in
623 the troctolites took place at hyper-solidus conditions (close to the solidus temperature of the
624 magmatic system). The high equilibration temperatures (1004 ± 20 ºC; Fig. 14) estimated on
625 the basis of the coexistence of clinopyroxene–orthopyroxene in one troctolite mylonite
626 confirm this hypothesis. We must note that these temperatures are very close to the stability
627 limit of pargasitic amphibole at low pressures, which is considered to be at temperatures
628 <1000 ºC (Koepke et al., 2004; 2005; 2007). Hence, one possibility is that the temperature
629 estimates for the mylonites give the crystallization temperature of an amphibole formed by a
630 melt present during the deformation process. The chemical modifications in the neoblastic
631 plagioclase of the sheared troctolite in Figure 7a, which has lower anorthite compared to that
632 of the porphyroclasts (An_{78} and An_{81} respectively) may also suggests that the granulite facies
633 deformation in the mylonites might have occurred in the presence of interstitial melt.

634 Although this idea would need to be better constrained by a more thorough chemical
635 characterization of the porphyroclastic and neoblastic minerals in the mylonites, the
636 occurrence of melts at the onset granulite-grade deformation is consistent with the
637 composition of the two ultramylonites shown in Figure 6. Both cases show a clear variation
638 in the neoblastic assemblage crystallized during the strain localization from the proto-

mylonite to the ultramylonite zone. In particular, although they are hosted in mineralogically different mylonites, both ultramylonites are formed by anorthitic plagioclase (An_{65} to An_{82}), Ti-rich pargasitic amphibole (TiO_2 1.7–3.7 wt.%), and minor clinopyroxene (Mg# 75 to 85). In contrast to the host rocks (oxide gabbro and troctolite), they do not contain olivine, spinel or Ti-Fe oxides (Figs 6; 7). Felsic rocks containing plagioclase and amphibole are often found in abyssal and ophiolitic gabbros as crosscutting veins or discrete bodies associated with oxide-rich gabbros (Dick et al., 2000; Koepke et al., 2004; 2007; Tribuzio et al., 2014; MacLeod et al., 2017). These rocks are interpreted as the product of crystallization of silica-rich melts produced by extreme fractional crystallization of MOR-type basalt and/or partial melting of hydrothermally altered gabbro (see discussion in Tribuzio et al., 2014). Hence, one can argue that the ultramylonites represent the recrystallization of felsic material originally located within the host rock and mylonitized during the deformation event. However, this is at odds with the high anorthite in plagioclase (An_{83}-An_{65}) and Mg# in clinopyroxene and amphibole (Mg# 75–85 and 67–80 respectively) in the ultramylonites. In addition, the composition of the amphibole in the ultramylonite formed from a troctolite progenitor is similar to that of the amphibole in the host rock (Figure 10b). The temperature estimates for the amphibole-plagioclase couples in the ultramylonite furnish very high values ranging from 930 ºC and ~1020 ºC, comparable to those in the host mylonites (Fig. 14). Based on these data, it is plausible that the ultramylonite layers may represent melt-rich zones developed during the same deformation event as the host granulite-facies mylonites. The peculiar mineralogical and chemical compositions of these layers indicate that the melt had a hybrid composition, i.e., high Mg/Fe and Ca/Na ratios, but rich in silica, incompatible elements and water. The ultramylonite hosted in an oxide-gabbro, has plagioclase showing a strong increase in anorthite component (~82 mol.%) compared to that in the host mylonite (~46 mol.%). The high anorthite is also ascribable to the occurrence of a water-bearing melt during the crystallization of the neoblastic plagioclase (Berndt et al., 2005). Further investigation will shed light on the nature of this hybrid melt and the mechanism that allowed the strain localization to form the ultramylonite.

667 In summary, our data suggest that the granulite facies deformation event recorded by
668 the gabbros occurred shortly after the crystallization of the magmatic phases. This event my
669 have possibly enhanced the expulsion of the liquid from the crystal framework, allowing the
670 formation of oxide-rich seams within the gabbros and/or discrete oxide-rich horizons often
671 associated with high-temperature deformation. A similar process has been proposed by
672 Natland and Dick (2001) to explain the close association of oxide-rich layers and granulite-
673 grade mylonites in gabbros from Hole 735B at Atlantis Bank. We note though that
674 thermometry estimates of the mylonites analyzed by Miranda and John (2010) from Hole
675 735B yielded temperatures <910ºC generally lower than those reported in the present study.
676 Nonetheless, the occurrence of high-temperature ultramylonites likely formed in the presence
677 of melt suggests a complex interplay between deformation and melt percolation that has also
678 been proposed for mylonitic rocks drilled at the inside-corner high of the MAR at 23°N
679 (Agar and Lloyd, 1997).
680
681 **5.3 Hydrothermal alteration**
682 Distinctive black hornblende-rich veins locally crosscut the gabbros at high angle to the high-
683 temperature metamorphic foliation of the host rock. These vein-filled fractures represent
684 formation during brittle deformation that is also related to the crystallization of hornblende
685 pseudomorphs after the magmatic clinopyroxene in the host rock, indicating the host gabbros
686 enjoyed migration of hydrous fluids from the vein into the gabbro. This process also accounts
687 for the formation of secondary plagioclase (albitic in composition) crystallizing within
688 microcracks connecting the different amphibole pseudomorphs.

689 Both the vein and clinopyroxene pseudomorph hornblende in the gabbros have
690 appreciable Cl contents (0.1–0.2 wt.%) similar to that in hydrothermal amphiboles in other
691 abyssal gabbros (Coogan et al., 2001; Cortesogno et al., 2004; Tribuzio et al., 2016). This
692 suggests that both amphibole types formed by interaction with water-rich fluids likely derived
693 from seawater (see also Alt and Bach 2006). However, the amphibole from the veins has lower
694 Mg# (70–77) and higher TiO_2 contents (3.0–3.3 wt.%) compared to the coronitic hornblende

adjacent to the veins in the gabbro (Mg# = 75–81; TiO_2 <1.5 wt.%), approaching the Ti and Al of the magmatic pargasite in the troctolites (Fig. 10). The chemical map in Figure 7d shows that the hornblende statically replacing the pyroxene is associated with fine-grained plagioclase having very low anorthite contents (20–25 mol.%) and is typically found in microcracks. Temperature estimates based on plagioclase-amphibole pairs yield amphibolite facies temperatures of ~700 ºC (Fig. 14). This suggests that the hornblende replacing the clinopyroxene likely formed by interaction of the magmatic phases with seawater-derived fluids (Coogan et al., 2001), which caused the recrystallization of Na-rich plagioclase within cracks and microveins (see also Tribuzio et al., 2016). On the other hand, the high Ti and Al in the hornblende from the veins suggest that magmatic components were likely still present within the fluids forming these veins. This is in agreement with the high temperature (920–970 ºC) indicated by the plagioclase-amphibole thermometers on a euhedral plagioclase contained in the vein. The occurrence of magmatic components in the hornblende-rich veins was also inferred for the amphibole-rich veins crosscutting gabbro at Atlantis Bank (Alt and Back, 2006) and in the Ligurian ophiolites (Tribuzio et al., 2014) and related to fluids exsolved from highly evolved melts residual from the magmatic differentiation process.

In summary, the microtextures and the chemical variability of the amphibole forming the hydrothermal hornblende offer a snapshot to the retrograde evolution of this portion of the lower crust exhumed by a detachment fault. In line with previous studies on abyssal and ophiolitic gabbros, we propose that a magmatic component was still present during the first stages of hydrothermal alteration at the ductile-brittle transition. This stage was followed by further cooling, by the ingress of seawater along cracks and by the static replacement of the magmatic phases by green hornblende and albitic plagioclase.

6. CONCLUSIONS

The lower oceanic crust exposed in the 16.5 ºN region of the Mid-Atlantic Ridge formed in a detachment fault system characterized by a moderate to low magma supply. Dredge hauls indicate a bimodal composition of the lower crust that is formed by a high proportion of

723 dunites and troctolites associated with evolved gabbronorites and oxide gabbros, and a lack
724 of intermediate rock types. Using a thermodynamic model, we infer that a similar bimodal
725 distribution of the lower oceanic crust is expected in regions where gabbroic intrusions are
726 scattered within partly serpentinized mantle peridotite. The formation of these "ephemeral"
727 magma chambers within the mantle lithosphere causes a high eruption rate, which in turn
728 allows most of the melt to be erupted after moderate degrees of fractionation. This idea is
729 also consistent with the evidence that small amounts of melt were present at the onset of the
730 high-temperature deformation related to the oceanic detachment. The development of
731 porphyroclastic to mylonitic fabrics occurred at near-solidus conditions (~1000 ºC) and was
732 likely associated with the expulsion of interstitial, evolved melts from the crystal matrix.
733 This mechanism enhanced the formation of disconnected oxide-gabbro seams or layers often
734 associated with crystal-plastic fabrics in the host gabbros. The high-temperature deformation
735 was followed by hydrothermal alteration marked by the formation of amphibole-rich veins at
736 high-temperature conditions (~900 ºC). This study suggests that the compositional variability
737 of the lower oceanic crust formed at the 16.5 ºN region of the Mid-Atlantic Ridge is the
738 consequence of the complex interplay between low melt supply and high-temperature
739 deformation representing the deep expression of the detachment fault.
740

741 **ACKNOWLEDGMENTS**

742 The geochemical data used in this study and the parameters of the model are included as Tables
743 in the Supplementary Material. The data published will be contributed to the Petrological
744 Database (www.earthchem.org/petdb). We thank the captain and crew of the R/V Knorr for
745 their help and enthusiasm during our cruise to the 16.5º core complexes. Deborah Smith served
746 as best chief scientist ever. Hans Schouten and Joe Cann kept HJBD in line and together with
747 Vincent Salters, Ross Parnell-Turner, Fuwu Ji, Dana Yoerger, Camilla Palmiotto, A.
748 Zheleznov, H. L. Bai, and Will Junkin interpreted the geophysical data and described the rock
749 samples on which this paper is based. A.S was financially supported with an InterRidge
750 fellowship and by the *Societa' Italiana di Minerlogia e Petrografia*. HRM acknowledges

751 support from the Wilhelm und Else Heraeus Stiftung. HJBD acknowledges support from the
752 National Science Foundation grants MG&G 1155650 and MG&G 1434452, and discussions
753 and assistance in the laboratory from Ma Qiang. Fuwu Ji, Joe Cann, Deborah Smith, Hans
754 Schouten, and Ross Parnell-Turner assisted in dredging, sample description, and provide the
755 authors with considerable insight into the geologic and geophysical data collected during the
756 Knorr Cruise 210 Leg 5. Comments by E. Rampone, G Ceuleneer and an anonymous reviewer
757 improved the quality of the manuscript.
758

759 **FIGURE CAPTIONS**
760
761 **Figure 1.** Bathymetric map of the Mid-Atlantic Ridge, 16.5 ºN area studied by cruise, R/V
762 Knorr, KNR210-5 (Smith et al., 2014). The location of Southern, Central and Northern Core
763 complexes are also indicated.
764
765 **Figure 2. (A)** Location of the dredges collected during the cruise, R/V Knorr, KNR210-5
766 (Smith et al., 2014). Large pie diagrams refer to the dredges where gabbros or peridotites were
767 collected, dredge numbers are indicated. **(B)** Compositional variability of all lithologies and
768 plutonic rocks from Southern , Central (CC) and Northern Core Complexes (NCC).
769
770 **Figure 3.** Photographs of cut hand specimens of six different plutonic rocks recovered by
771 dredging during R/V Knorr cruise 210-5. Some of the samples show high-temperature crystal-
772 plastic deformation with protomylonitic, mylonitic and ultramylonitic fabrics. In one case, the
773 high-temperature deformation fabrics are cross-cut by lower-temperature brittle fractures and
774 amphibole veins. CPF refers to crystal-plastic fabric as defined in the text.
775
776 **Figure 4.** Microphotographs of selected samples. **(A)** Olivine oikocrysts showing rounded
777 grain boudaries against plagioclase in an undeformed troctolite; **(B)** Large clinopyroxene
778 oikocryst including subrounded olivine and plagioclase chadacryst in a troctolite; Ti-pargasitic
779 amphibole in a sheared troctolite (CPF 1) showing interstitial **(C)** and oikocrystic **(D)** habitus;
780 **(E)** Sheared gabbronorite cut by amphibole vein with diffuse boundaries. Clinopyroxene
781 locally shows partial replacement by amphibole (CPF 2); **(F)** Hornblende corona statically
782 replacing clinopyroxene in the vicinity of the amphibole vain in (**E**). Ol, olivine; Pl,
783 plagioclase; Cpx; clinopyroxene; Ti-Prg, Ti-pargasite; Hbl, horneblende.
784
785 **Figure 5**. Histogram of deformation intensity of plutonic rocks collected during R/V Knorr
786 cruise 210-5 (see text for detail).
787
788 **Figure 6.** Macroscopic occurrence and microphotographs of the amphibole-plagioclase
789 ultramylonites and host mylonites. (**A**) Troctolite showing a gradual increase in deformation
790 intensity from protogranular to mylonite to ultramylonite (UM). (**B**) Scanned thin-section
791 image of the ultramylonite band crosscutting an oxide-gabbro mylonite. Note that the texture
792 and the mineralogical composition of the two ultramylonites are almost identical, although they
793 are developed in highly different magmatic protoliths.
794
795 **Figure 7.** FEG-SEM compositional maps of selected samples. (**A**) Na, Ca and Mg map of a
796 sheared troctolite clearly showing an increase in Na and decrease in Ca in the neoblastic
797 plagioclase compared to the coexisting porphyroclasts. (**B**) Cr, Ca, Mg, S and Ti maps of the
798 troctolite mylonite including a Amp-Pl ultramylonitic band. The maps show a decrease in Ca in
799 plagioclase in the ultramylonite compared to the mylonite and the distribution of Ti-bearing
800 phases (i.e., amphibole) and Cr-bearing phases (i.e., spinel) between the two lithologies. (**C**) Na
801 and Ti map of the oxide-gabbro mylonite including a amphibole-plagioclase ultramylonitic
802 band. The maps show a sharp decrease in Na in plagioclase in the ultramylonite compared to
803 the mylonite and the lack of Ti-Fe oxides in the ultramylonite. (**D**) Detail of a Na, Mg and Fe
804 map of a gabbro crosscut by an amphibole vein. Note that hornblende replacement is
805 widespread in the vicinity of the amphibole vein, and that Na-rich plagioclase is associated
806 with micro-cracks and late fractures.
807
808
809 **Figure 8.** Variations in TiO_2 (**A**) and Cr_2O_3 (**B**) versus $Mg/(Mg+Fe^{2+})$ (mol.%) in
810 clinopyroxenes from the 16.5ºN gabbros. Symbols are grouped per rock-type and indicate
811 single spot analyses (core and rim). The composition of clinopyroxenes from gabbros from
812 other lower crustal sections exposed along the Mid-Atlantic Ridge are also depicted (Ross and
813 Elthon, 1993; Nonnotte et al., 2005; Coogan et al., 2002; Suhr et al., 2008; Drouin et al., 2009;
814 Lissenberg and Dick, 2008; Dick et al., 2010).

Figure 9. Covariations in clinopyroxene Mg/(Mg+Fe^{2+}) (mol.%) versus Ca/(Ca+Na) (mol.%) in plagioclase and Mg/(Mg+Fe^{2+}) (mol.%) in orthopyroxene coexisting in selected gabbros. Dashed arrows indicate the chemical variation in clinopyroxene and plagioclase in the ultramylonite compared to the host oxide-gabbro mylonite. Data are averaged per sample, error bars represent one standard deviation of the mean value.

Figure 10. Compositions of amphibole from selected gabbros. (**A**) Variations in alkali (Na+K) and TiO_2 (wt.%) versus Al^{IV} (apfu) in amphibole from selected gabbros. (**B**) Same plot as A including only core analyses of pargasite and brown horneblende. (**C**) Chlorine (wt.%) versus Al^{IV} (apfu) in amphibole; detection limit of EPMA analyses is also indicated. (**D**) Variations in TiO_2 (wt.%) versus Mg/(Mg+Fe^{2+}) (mol.%) in pargasite and brown-hornblende (core analyses). Each symbol represents a single spot analysis.

Figure 11. (**A**) Compositional distribution of basalts from Gakkel Ridge (~500 glass analyses); Mid-Atlantic Ridge 10–35 ºN (~1300 glass analyses); East Pacific Rise 9–13 ºE and East Pacific Rise 9–13 ºN (~230 glass analyses) and East Pacific Rise 14–20 ºN (~1050 glass analyses). Data compiled from PetDB (Lehnert et al., 2000). **(B)** Average compositions and standard deviation of Na_8 (Klein and Langmuir, 1987) versus Mg/(Mg+Fe) of the basalts in (A). The average full spreading rates of the regions are also indicated (see also Sinton and Detrick, 1992 and Coogan, 2007).

Figure 12. Visual explanation of the quantitative model. M1 is the primary melt with Mg/(Mg+Fe) ~72 and mass 100g. M2 to M13 are melts produced by the model at steps of Mg#~4. The mass of melt at each step is calculated as indicated by the italic numbers. B1 to B12 are melt extracted at each step of the model. Their mass is scaled to reproduce the actual compositional variability of melts erupted at the MAR (10-35ºN). G1 to G13 are gabbros produced by the model, and forming the "cumulate". T1 to T12 are melts trapped at each step and subtracted form the total melt mass. T_{tot} is the sum of T1 to T12 and is used to calculate the proportion of gabbros crystallized from trapped melts ("trapped"). The "Total" lower crust composition is given by the sum of gabbros crystallized as "cumulate" + "trapped" (see text for details).

Figure 13. Liquid Mg/(Mg+Fe) (mol.%) compositions versus (**A**) olivine Fo (black line and red circles) and clinopyroxene Mg/(Mg+Fe) (blue line and blue circles); (**B**) mass of gabbros (%) crystallized at each step of the thermodynamic model at different mass erupted /mass crystallized ratios (Me/Mc); (**C**) trapped melt (%) and (**D**) liquid density calculated at each step of the crystallization process. (**E**) Compositional variability of gabbros resulted from the thermodynamic model. The origin represents the mass of gabbros neglecting eruption, on the x-axis are depicted the model outcomes for different Me/Mc ratios if melt entrapment is ignored. The effect of melt entrapment is shown in the pie diagrams displayed vertically. The vertical displacement of each diagram depends on the total amount of trapped melt, as represented on the y-axis. The grey dashed line connects model results for different trapped melt compositions (see text for details). The compositional variability of the gabbros dredged at the MAR 16.5ºN region, and those from the hole U1309 at the Atlantis Massif (Blackman et al., 2011) are also reported. (**F**) Compositional variability of the basalts erupted at different Me/Mc ratios compared to the basalts from the MAR 10–35ºN segment.

Figure 14. Temperature estimates calculated using the edenite-richterite amphibole-plagioclase thermometer (Holland & Blundy,1994) assuming a pressure of 200 MPa. Mean values and standard deviations are given for individual textural amphibole-plagioclase types for each sample.

869 **REFERENCES**

870 Agar, S.M., G.E. Lloyd (1997), Deformation of Fe-Ti oxides in gabbroic shear zones from the
871 MARK area, in: Karson, J.A., Cannat, M., Miller, D.J., Elthon, D. (Eds.), Proceedings of the
872 Ocean Drilling Program, Scientific Results. Ocean Drilling Program, College Station, TX,
873 pp. 123-135.

874 Alt, J. C., W. Bach (2006), Oxygen isotope composition of a section of lower oceanic crust,
875 ODP Hole 735B, Geochem. Geophys. Geosys., 7, Q12008. http://dx.doi.org/10.1029/
876 2006GC001385.

877 Blackman, D. K., B. Ildefonse, B. E. John, Y. Ohara, D. J. Miller, C. J. MacLeod, and
878 Expedition 304/305 Scientists (2006), Oceanic core complex formation, Atlantis Massif,
879 Proceedings of Integrated Ocean Drilling Program, 304/305, 304, 605 pp., Ocean Drill.
880 Program, College Station, Tex., doi:10.2204/iodp.proc.304305.2006.

881 Blackman, D.K., Collins, J.A., 2010. Lower crustal variability and the crust/mantle transition at
882 the Atlantis Massif oceanic core complex. Geophysical Research Letters 37, 5 pp.

883 Blackman DK, Ildefonse B, John BE et al. (2011) Drilling constraints on lithospheric accretion
884 and evolution at Atlantis Massif, Mid-Atlantic Ridge 30°N, J Geophys Res, 116,25

885 Buck, W. R., L. L. Lavier and A. N. B. Poliakov (2005), Modes of faulting at mid-ocean ridges,
886 Nature, 434, 719–723.

887 Borghini G., E. Rampone (2007), Postcumulus processes in oceanic-type olivine-rich
888 cumulates: the role of trapped melt crystallization versus melt/rock interaction, Contrib
889 Mineral Petrol 154:619–633

890 Cann, J. R., D. K. Blackman, D. K. Smith, E. McAllister, B. Janssen, S. Mello, E. Avgerinos,
891 A. R. Pascoe, and J. Escartın (1997), Corrugated slip surfaces formed at North Atlantic
892 ridge-transform intersections, Nature, 385, 329–332.

893 Cannat, M. (1993), Emplacement of mantle rocks in the seafloor at mid-ocean ridges, J.
894 Geophys. Res., 98, 4163–4172, doi:10.1029/92JB02221.

895 Cannat, M., J.F. Casey, J.F. (1995). An Ultramafic Lift at the Mid-Atlantic Ridge: Successive
896 Stages of Magmatism in Serpentinized Peridotites from the 15 degree N Region, in: Vissers,
897 R., Nicolas, A. (Eds.), Mantle and Lower Crust Exposed in Oceanic Ridges and in

898 Ophiolites. Kluwer, Norwell, Massachusetts, pp. 5-34.
899 Cannat, M., Y. Lagabrielle, H. Bougault, J. Casey, N. de Coutures, L. Dmitriev,Y. Fouquet,,
900 (1997). Ultramafic and gabbroic exposures at the Mid-Atlantic Ridge: geologic mapping in
901 the 15°N region. Tectonophysics 279, 193-213.
902 Cannat, M., D. Sauter, V. Mendel, E. Ruellan, K. Okino, J. Escartin, V. Combier, and M. Baala
903 (2006), Modes of seafloor generation at a meltpoor ultraslow-spreading ridge, Geology,
904 34(7), 605–608.
905 Coogan L (2007), The lower oceanic crust. In: Turekian KK, Holland KD (eds) Treatise on
906 geochemistry, vol 3.19. Elsevier, Amsterdam, pp 1–45
907 Coogan L.A., A.D. Saunders, P.D. Kempton, M.J. Norry (2000), Evidence from oceanic
908 gabbros for porous melt migration within a crystal mush beneath the Mid- Atlantic Ridge,
909 Geochem Geophys Geosys, 1(9). doi:10.1029/2000GC000072
910 Coogan L. A., R. N. Wilson, K. M. Gillis and C.J., MacLeod (2001), Near-solidus evolution of
911 oceanic gabbros: insights from amphibole geochemistry, Geochim. Cosmochim. Acta, 65,
912 4339–4357.
913 DeMets, C., R. G. Gordon, and D. F. Argus (2010), Geologically current plate motions,
914 Geophys. J. Int., 181, 1–80.
915 Dick, H. J. B., Bryan, W. B. & Thompson, G. (1981). Low-angle faulting and steady-state
916 emplacement of plutonic rocks at ridge-transform intersections. EOS 62, 406.
917 Dick, H.J.B., J.H. Natland (1996), Late-stage melt evolution and transport in the shallow
918 mantle beneath the East Pacific Rise. Proceedings of the Integrated Ocean Drilling Program,
919 147, pp. 103–134.
920 Dick H.J.B., J.H. Natland, J.C. Alt, W. Bach, D. Bideau and Expedition Scientists (2000), A
921 long in situ section of the lower ocean crust: results of ODP Leg 176 drilling at the
922 Southwest Indian Ridge, Earth and Planetary Science Letters, 179, 31–51.
923 Dick, H. J. B., M. A. Tivey, and B. E. Tucholke (2008), Plutonic foundation of a slow-
924 spreading ridge segment: Oceanic core complex at Kane Megamullion, 23300N, 45200W,
925 Geochem. Geophys. Geosyst., 9, Q05014, doi:10.1029/2007GC001645.

926 Drouin M., M. Godard, B. Ildefonse, O. Bruguier, C.J. Garrido (2009), Geochemical and
927 petrographic evidence for magmatic impregnation in the oceanic lithosphere at Atlantis
928 Massif, Mid-Atlantic Ridge (IODP Hole U1309D, 30°N), Chem Geol 264:71–88
929 Drouin, M., B. Ildefonse, M. Godard (2010), A microstructural imprint of melt impregnation in
930 slow-spread lithosphere: olivine-rich troctolites from the Atlantis Massif (Mid-Atlantic
931 Ridge 30°N, IODP Hole U1309D). Geochem Geophys Geosyst, 11:Q06003.
932 doi:10.1029/2009GC002995
933 Escartın, J., D. K. Smith, J. Cann, H. Schouten, C. H. Langmuir, and S. Escrig (2008), Central
934 role of detachment faults in accretion of slow-spread oceanic lithosphere, Nature, 455, 790–
935 794, doi:10.1038/nature07333.
936 Gao, Y., J. Hoefs, E. Hellebrand, A. von der Handt, Snow (2007), Trace element zoning in
937 pyroxenes from ODP Hole735B gabbros: diffusive exchange or synkinematic crystal
938 fractionation?, Contrib Mineral Petrol 153:429–442
939 Ghiorso, M. S., M.M. Hirschmann, P.W Reiners, and V.C.I. Kress (2002). The pMELTS: A
940 revision of MELTS aimed at improving calculation of phase relations and major element
941 partitioning involved in partial melting of the mantle at pressures up to 3 GPa,
942 Geochemistry, Geophysics, Geosystems 3, doi:10.1029/2001GC000217.
943 Ghiorso, M.S., O., Sack (1995), Chemical mass transfer in magmatic processes, IV, A revised
944 and internally consistent thermodynamic model for the interpolation and extrapolation of
945 liquid-solid equilibria in magmatic systems at elevated temperatures and pressures,
946 Contribution to Mineralogy and Petrology 119, 197–212.
947 Gillis K.M., J. Snow et al. (2014) Primitive layered gabbros from fast-spreading lower oceanic
948 crust. Nature, 505, 204-207.
949 Godard, M., Awaji, S., Hansen, H., Hellebrand, E., Brunelli, D., Johnson, K., Yamasaki, T.,
950 Maeda, J., Abratis, M., Christie, D., Kato, Y., Mariet, C., and Rosner (2009), Geochemistry
951 of a long in-situ section of intrusive slow-spread oceanic lithosphere: results from IODP Site
952 U1309 (Atlantis Massif, 30°N Mid-Atlantic-Ridge), Earth and Planetary Science Letters,
953 279, 110–122.

954 Hansen, L.N., M.J. Cheadle, B.E. John, S.M. Swapp, H.J.B. Dick, B.E. Tucholke and M.A.
955 Tivey (2013), Mylonitic deformation at the Kane oceanic core complex: implications for the
956 rheological behavior of oceanic detachment faults, Geochemistry, Geophysics, Geosystems,
957 14, 3085–3108.
958 Holland, T., J. Blundy (1994), Non-ideal interactions in calcic amphiboles and their bearing on
959 amphibole-plagioclase thermometry, Contrib. Mineral. Petrol. 116, 433–447.
960 Ildefonse, B., D. K. Blackman, B. E. John, Y. Ohara, D. J. Miller, and C. J. MacLeod (2007),
961 Oceanic core complexes and crustal accretion at slow-spreading ridges, Geology, 35, 623–
962 626, doi:10.1130/G23531A.1.
963 Karson, J. A., Dick H. J. B. (1983). Tectonics of ridge-transform intersections at the Kane
964 Fracture Zone. Marine Geophysical Researches 6, 51-98.
965 Kinzler R.J., T.L. Grove (1993), Corrections and further discussion of the primary magmas of
966 mid-ocean ridge basalts, 1 and 2, J Geophys Res, 98, 22339–22347.
967 Klein EM, C.H. Langmuir (1987), Global correlation of ocean ridge basalt chemistry with axial
968 depth and crustal thickness, J Geophys Res, 92, 8089–8115
969 Koepke J., S. T.Feig, J. Snow and M. Freise (2004), Petrogenesis of oceanic plagiogranites by
970 partial melting of gabbros: an experimental study. Contrib. Mineral. Petrol, 146, 414–432.
971 Koepke J., Berndt, S.T. Feig and F. Holtz (2007), The formation of SiO2-rich melts within the
972 deep oceanic crust by hydrous partial melting of gabbros, Contrib. Mineral. Petrol, 153, 67–
973 84.
974 Lehnert, K., Su, Y., Langmuir, C. H., Sarbas, B. and U. Nohl (2000), A global geochemical
975 database structure for rocks, Geochemistry, Geophysics, Geosystems 1,
976 doi:10.1029/1999GC000026.
977 Lindsley, D. H., and B. R. Frost (1992), Equilibria among Fe-Ti oxides, pyroxenes, olivine, and
978 quartz: Part I. Theory, Am. Mineral., 77, 987–1003.
979 Lissenberg C.J., H.J.B. Dick (2008), Melt–rock reaction in the lower oceanic crust and its
980 implications for the genesis of mid-ocean ridge basalt, Earth Planet Sci Lett, 271, 311–325
981 Lissenberg C.J., K.A. Howard, C.J. MacLeod, M. Godard (2013), Pervasive reactive melt

migration through fast-spreading lower oceanic crust (Hess Deep, equatorial Pacific Ocean), Earth Planet Sci Lett 361:436–447

Lissenberg, C. J., C. MacLeod (2016), A reactive porous flow control on Mid-ocean Ridge magmatic evolution, J Petrol, 57, 2195–2220

MacLeod, C. J., R. C. Searle, B. J. Murton, J. F. Casey, C. Mallows, S. C. Unsworth, K. L. Achenbach, and M. Harris (2009), Life cycle of oceanic core complexes, Earth Planet Sci. Lett., 287, 333–344.

MacLeod C.J.,H.J.B. Dick, P. Blum, N. Abe, D.K. Blackman (2017), Site U1473. In MacLeod, C.J., Dick, H.J.B., Blum, P., and the Expedition 360 Scientists, Southwest Indian Ridge Lower Crust and Moho, Proceedings of the International Ocean Discovery Program, 360: College Station, TX (International Ocean Discovery Program).

Mehl, L., and G. Hirth (2008), Plagioclase preferred orientation in layered mylonites: Evaluation of flow laws for the lower crust, J. Geophys. Res., 113, B05202, doi:10.1029/2007JB005075.

Melson W.G., T.L. Vallier, T.L. Wright, G. Byerly and J. Nelson (1976), Chemical diversity of abyssal volcanic glass erupted along Pacific, Atlantic, and Indian Ocean sea-floor spreading centers. In: The Geophysics of the Pacific Ocean Basin and Its Margin (AGU, Washington), p 351–367

Mendel, V., Sauter, D., Parson, L., Vanney, J. R. (1997). Segmentation and morphotectonic variations along a super slow-spreading center: The Southwest Indian Ridge (57 degrees E-70 degrees E). Marine Geophysical Researches 19, 505-533.

Meyer P.S., H.J.B. Dick, G. Thompson (1989), Cumulate gabbros from the Southwest Indian Ridge, 548S^78160E: implications for magmatic processes at a slow spreading ridge. Contrib Miner Petrol, 103:44–63

Miranda E.A., and B.E. John (2010), Strain localization along the Atlantis Bank oceanic detachment fault system, Southwest Indian Ridge, Geochemistry, Geophysics, Geosystems, 11(4):Q04002.

Morse SA (1979), Kiglapait geochemistry II. Petrography, J Petrol, 20, 591-624

1010 Natland, J.H. and H.J.B. Dick (2001), Formation of the lower ocean crust and the
1011 crystallization of gabbroic cumulates at a very slowly spreading ridge. Journal of
1012 Volcanology and Geothermal Research, 110, 191–233.
1013 Nonnotte P., Ceuleneer G. and Benoit M. (2005) Genesis of andesitic-boninitic magmas at mid-
1014 ocean ridges by melting of hydrated peridotites : geochemical evidence from DSDP Site 334
1015 gabbronorites. Earth Planet. Sci. Lett., 236, 632-653.
1016 Olive, J.-A., M. D. Behn, and B. E. Tucholke (2010), The structure of oceanic core complexes
1017 controlled by the depth distribution of magma emplacement, Nat. Geosci., 3, 491–495,
1018 doi:10.1038/ngeo888.
1019 Parnell-Turner, R., H. Schouten, D.K. Smith, (2016), Tectonic structure of the Mid-Atlantic
1020 Ridge near 16º30'N. Geochem. Geophys. Geosyst. https://doi .org /10 .1002
1021 /2016GC006514.
1022 Parnell-Turner, R., J. Escartin, J.A. Olive, D.K. Smith, S. Petersen (2018) Genesis of
1023 corrugated fault surfaces by strain localization recorded at oceanic detachments, Earth and
1024 Planetary Science Letters, 498, 116–128.
1025 Rampone E., G. Borghini, M. Godard, B. Ildefonse, L. Crispini and P. Fumagalli (2016)
1026 Melt/rock reaction at oceanic peridotite/ gabbro transition as revealed by trace element
1027 chemistry of olivine. Geochim. Cosmochim. Acta, 190, 309-331
1028 Reston, T. J., and C. R. Ranero (2011), The 3-D geometry of detachment faulting at mid-ocean
1029 ridges, Geochem. Geophys. Geosyst., 12, Q0AG05, doi:10.1029/2011GC003666
1030 Ross K. and Elthon D. (1993). Cumulates from strongly depleted mid-ocean ridge basalts.
1031 Nature, 365, 826-829.
1032 Sanfilippo A, Tribuzio R (2013) Origin of olivine-rich troctolites from the oceanic lithosphere:
1033 a comparison between the Alpine Jurassic ophiolites and modern slow spreading ridges,
1034 Ofioliti, 38, 89–99
1035 Sanfilippo A, H.J.B. Dick HJB, Y. Ohara (2013), Melt-rock reaction in the mantle: mantle
1036 troctolites from the Parece Vela ancient back-arc spreading center, J Petrol, 54,861–885
1037 Sanfilippo A., T. Morishita, H. Kumagai, K. Nakamura, K. Okino, K. Hara, A. Tamura, S. Arai

(2015), Hybrid troctolites from Mid-Ocean ridge, inherited mantle in the lower crust, Lithos, 232, 124–130

Sanfilippo A., H.J.B. Dick, Y. Ohara and M. Tiepolo (2016a) New insights on the origin of troctolites from the breakaway area of the Godzilla Megamullion (Parece Vela back-arc basin): The role of melt-mantle interaction on the composition of the lower crust, Island Arc, 25, 220-234, DOI: 10.1111/iar.12137

Sanfilippo, A., T. Morishita, R. Senda, (2016b). Rhenium-osmium isotope fractionation at the oceanic crust-mantle boundary. Geology, 44, 167-170. DOI: 10.1130/G37428.1

Sauter, D., Patriat, P., Rommevaux-Jestin, C., Cannat, M., Briais, A., Gallieni Shipboard Scientific Party. (2001). The Southwest Indian Ridge between 49°15'E and 57°E: focused accretion and magma redistribution. Earth and Planetary Science Letters 192, 303-317.

Schroeder, T. J., M. Cheadle, H. J. B. Dick, U. Faul, J. F. Casey, and P. B. Kelemen (2007), Non-volcanic seafloor spreading and corner-flow rotation accommodated by extensional faulting at 15ºN on the Mid Atlantic Ridge: A structural synthesis of ODP Leg 209, Geochem. Geophys. Geosyst., 8, Q06015, doi:10.1029/2006GC001567.

Sinton, J. M. and R.S. Detrick, (1992), Mid-Ocean Ridge magma chambers, Journal of Geophysical Research 97, 197-216.

Smith, D. K., J. Escartin, M. Cannat, M. Tolstoy, C.G. Fox, D. Bohnenstiehl, and S. Bazin (2003), Spatial and temporal distribution of seismicity along the northern Mid-Atlantic Ridge (15o235oN), J. Geophys. Res, 108(B3), 2167, doi:10.1029/2002JB001964.

Smith, D. K., J. R. Cann, and J. Escartin (2006), Widespread active detachment faulting and core complex formation near 13oN on the Mid-Atlantic Ridge, Nature, 442, 440–443, doi:10.1038/nature04950.

Smith, D.K., H. Schouten, H.J.B. Dick, J. Cann, V. Salters, H. Marschall, F. Ji, A. Yoerger, A. Sanfilippo, R. Parnell-Turner, C. Palmiotto, A. Zheleznov, H. Bai, H., W. Junkin, B.M. Urann, S. Dick, M. Sulanowska, P. Lemmond, S. Curry (2014), Development and evolution of detachment faulting along 50km of the Mid-Atlantic Ridge near 16.5◦N. Geochem. Geophys. Geosyst.15, 4692–4711. https://doi .org /10 .1002 /2014GC005563.

1066 Smith, D. K., J. Escartin, H. Schouten, and J. R. Cann (2008), Fault rotation and core complex
1067 formation: Significant processes in seafloor formation at slow-spreading mid-ocean ridges
1068 (Mid-Atlantic Ridge, 13–25oN), Geochem. Geophys. Geosyst., 9, Q03003,
1069 doi:10.1029/2007GC001699.
1070 Standish, J. J., Dick, H. J. B., Michael, P. J., Melson, W. G., O'Hearn, T. (2008), MORB
1071 generation beneath the ultraslow-spreading Southwest Indian Ridge (9°-25°E): Major
1072 element chemistry and the importance of process versus source. Geochemistry, Geophysics,
1073 Geosystems 9, 39 p.
1074 Stolper E. and D. Walker (1980), Melt Density and the Average Composition of Basalt,
1075 Contrib. Mineral. Petrol. 74, 7-12
1076 Tribuzio R., M. Tiepolo and M.F. Thirlwall (2000), Origin of titanian pargasite in gabbroic
1077 rocks from the Northern Apennine ophiolites (Italy): insights into the late-magmatic
1078 evolution of a MOR-type intrusive sequence, Earth and Planetary Science Letters, 176, 281–
1079 293.
1080 Tribuzio R., M.M. Renna, L. Dallai and A. Zanetti (2014), The magmatic–hydrothermal
1081 transition in the lower oceanic crust: Clues from the Ligurian ophiolites, Italy, Geochimica
1082 et Cosmochimica Acta 130, 188-211
1083 Tucholke, B. E., Lin, J. & Kleinrock, M. C. (1998), Megamullions and mullion structure
1084 defining oceanic metamorphic core complexes on the mid-Atlantic ridge. Journal of
1085 Geophysical Research-Solid Earth 103, 9857-9866.
1086 Tucholke, B. E., M. D. Behn, W. R. Buck and J. Lin (2008), Role of melt supply in oceanic
1087 detachment faulting and formation of megamullions, Geology, 36, 455–458.

Figure 1.

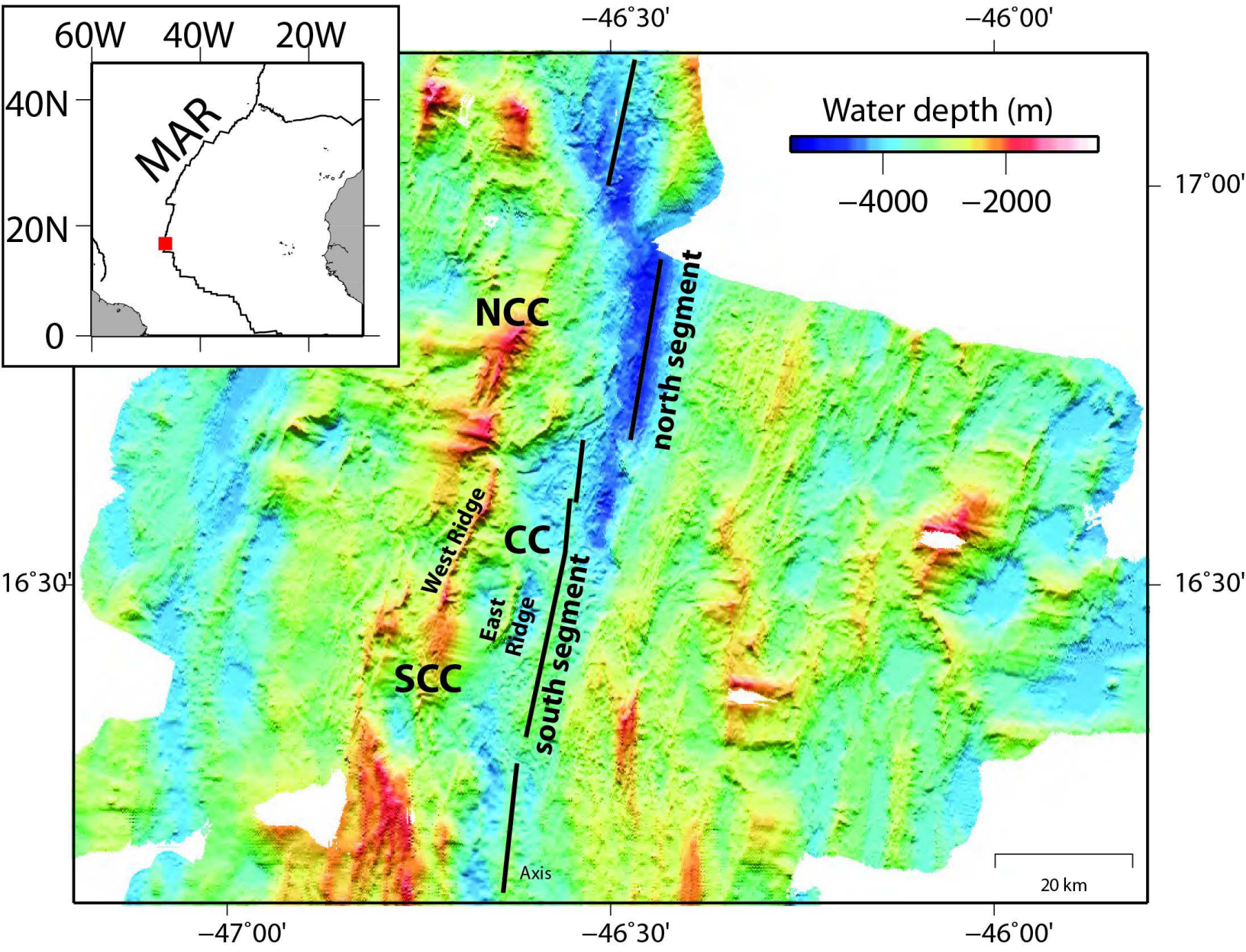
60W
40W
20W
40N
20N
0
MAR
−46°30'
−46°00'
17°00'
16°30'
−47°00'
Water depth (m)
−4000
−2000
NCC
north segment
West Ridge
CC
East Ridge
south segment
SCC
Axis
20 km

Figure 2.

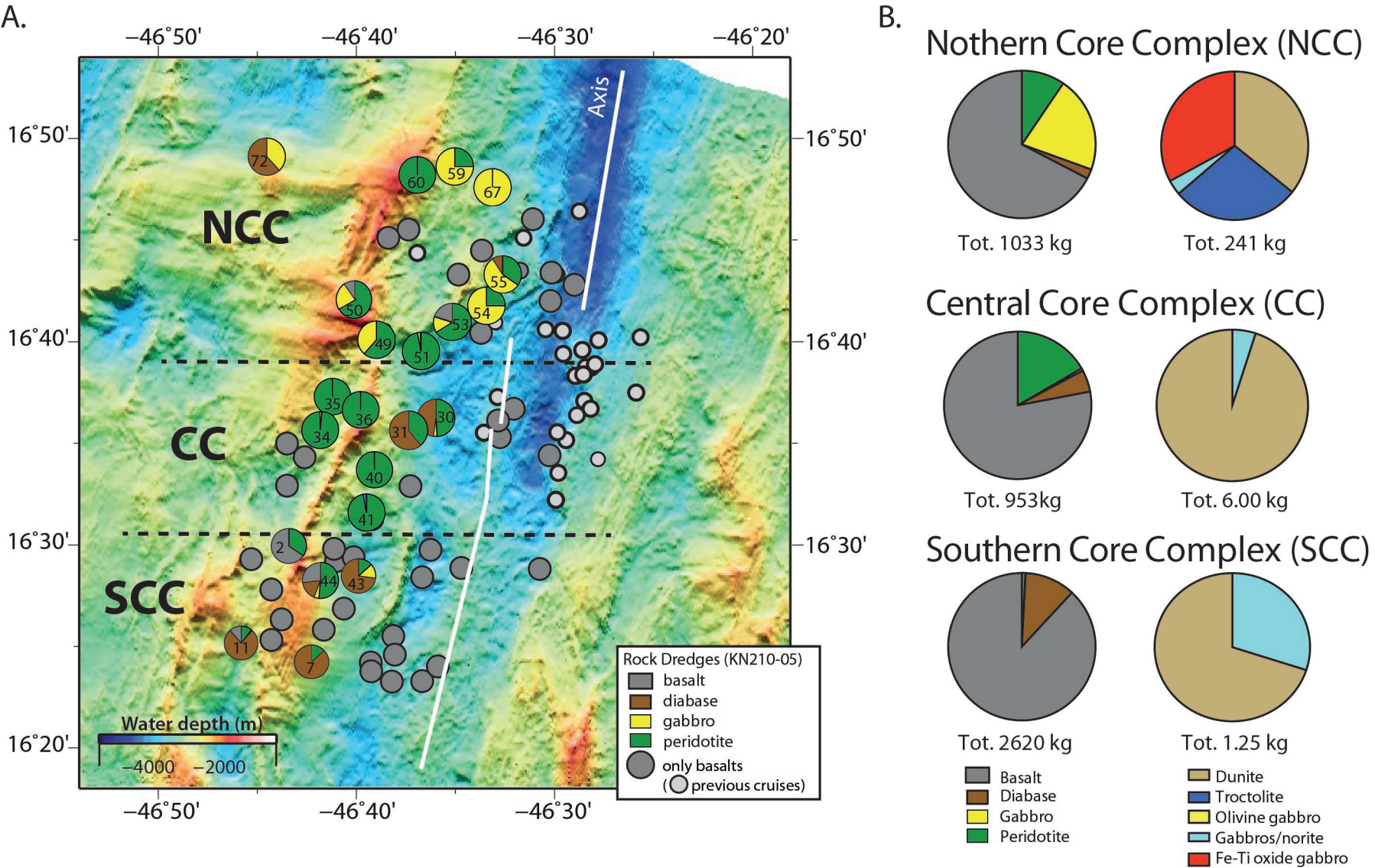
A.
−46°50'
−46°40'
−46°30'
−46°20'
16°50'
16°40'
16°30'
16°20'
NCC
CC
SCC
Axis
72
60
59
67
55
50
54
53
49
51
35
36
34
31
30
40
41
2
44
43
11
7
Water depth (m)
−4000
−2000
Rock Dredges (KN210-05)
basalt
diabase
gabbro
peridotite
only basalts
(previous cruises)
B.
Nothern Core Complex (NCC)
Tot. 1033 kg
Tot. 241 kg
Central Core Complex (CC)
Tot. 953kg
Tot. 6.00 kg
Southern Core Complex (SCC)
Tot. 2620 kg
Tot. 1.25 kg
Basalt
Diabase
Gabbro
Peridotite
Dunite
Troctolite
Olivine gabbro
Gabbros/norite
Fe-Ti oxide gabbro

Figure 3.

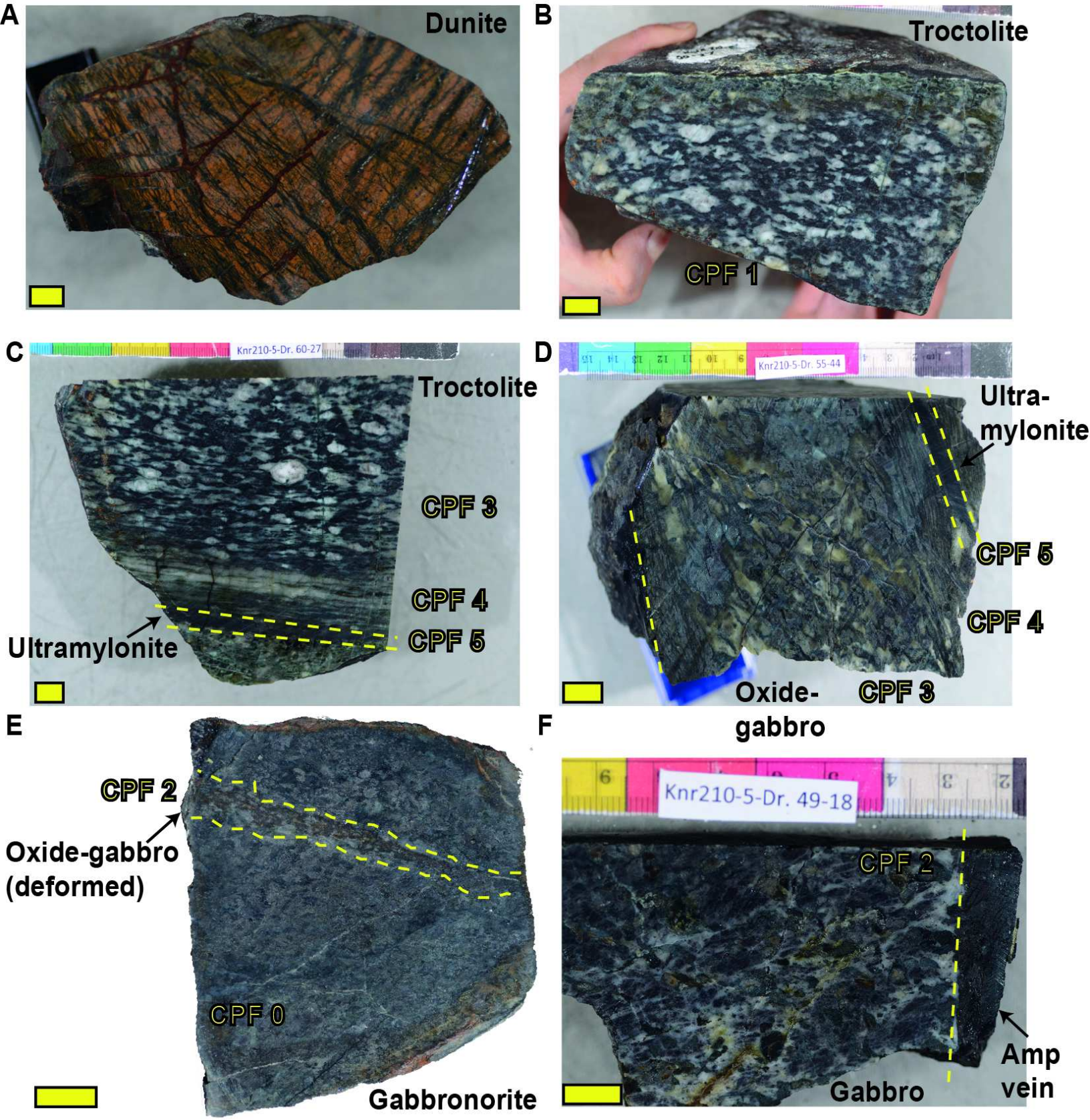
A
Dunite
B
Troctolite
CPF 1
C
Knr210-5-Dr. 60-27
Troctolite
CPF 3
CPF 4
CPF 5
Ultramylonite
D
Knr210-5-Dr. 55-44
Ultra-
mylonite
CPF 5
CPF 4
Oxide-
gabbro
CPF 3
E
CPF 2
Oxide-gabbro
(deformed)
CPF 0
Gabbronorite
F
Knr210-5-Dr. 49-18
CPF 2
Amp
vein
Gabbro

Figure 4.

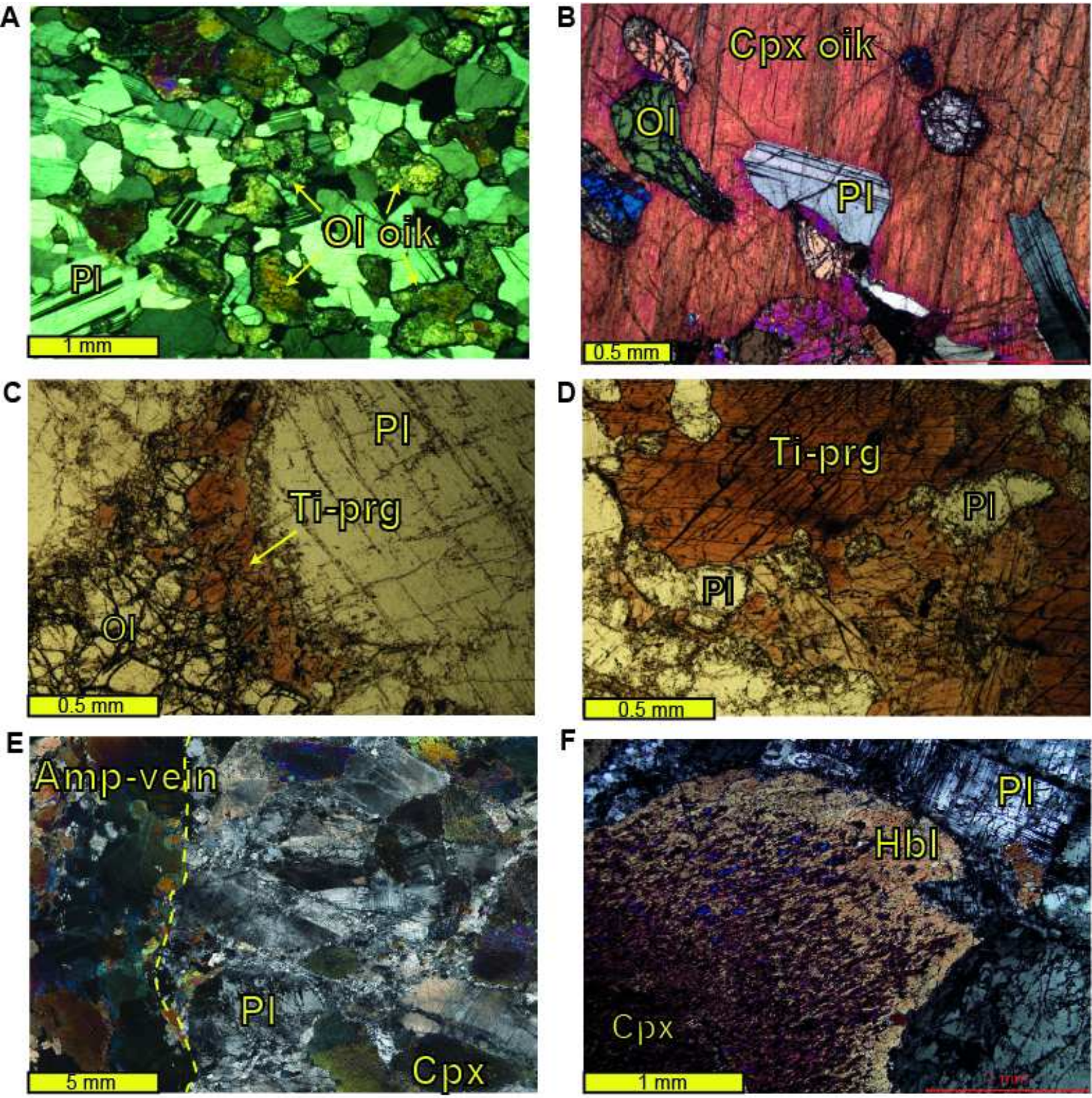
A
Ol oik
Pl
1 mm
B
Cpx oik
Ol
Pl
0.5 mm
C
Pl
Ti-prg
Ol
0.5 mm
D
Ti-prg
Pl
Pl
0.5 mm
E
Amp-vein
Pl
Cpx
5 mm
F
Pl
Hbl
Cpx
1 mm

Figure 5.

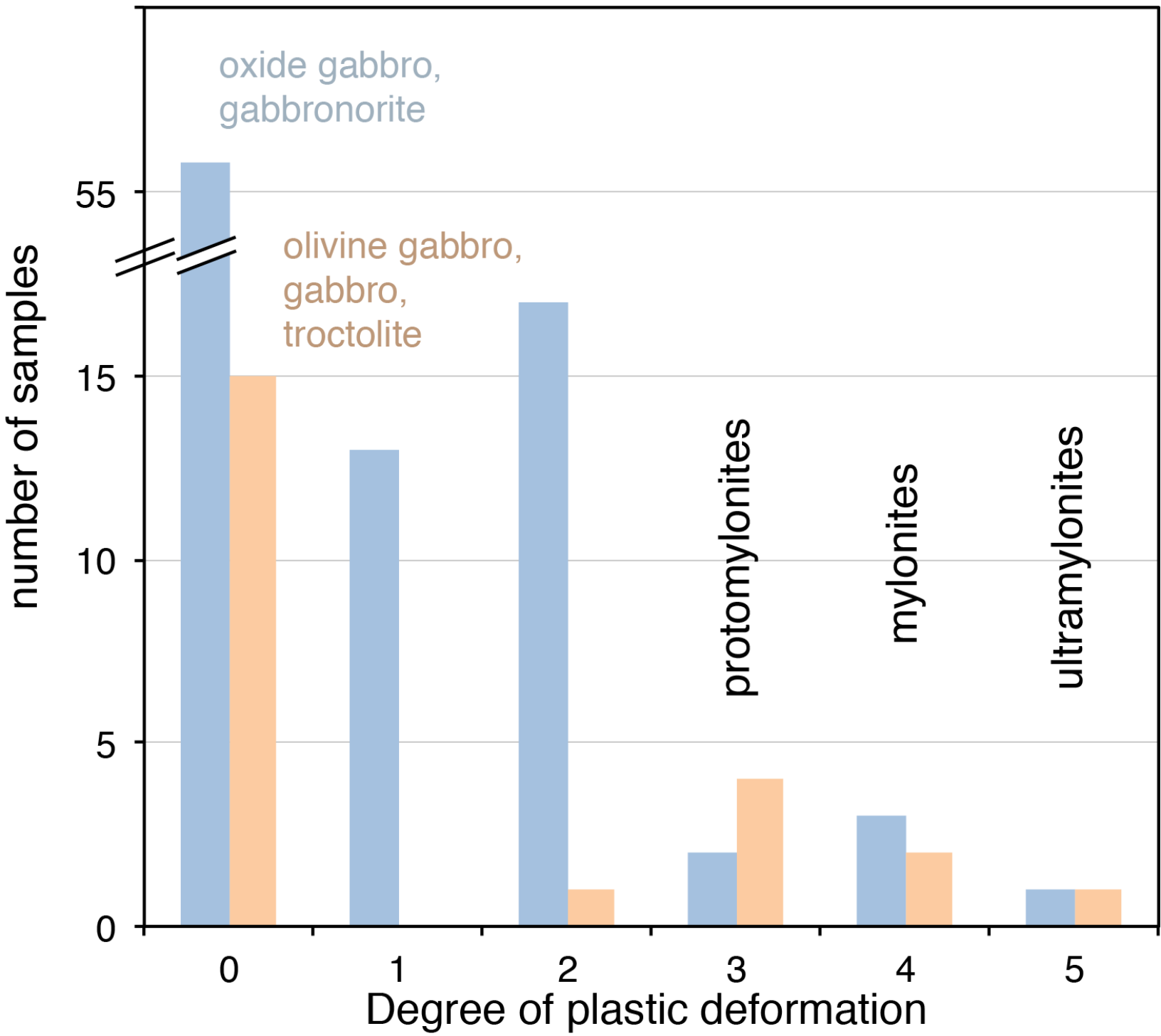
oxide gabbro,
gabbronorite
olivine gabbro,
gabbro,
troctolite
protomylonites
mylonites
ultramylonites
number of samples
55
15
10
5
0
0
1
2
3
4
5
Degree of plastic deformation

Figure 6.

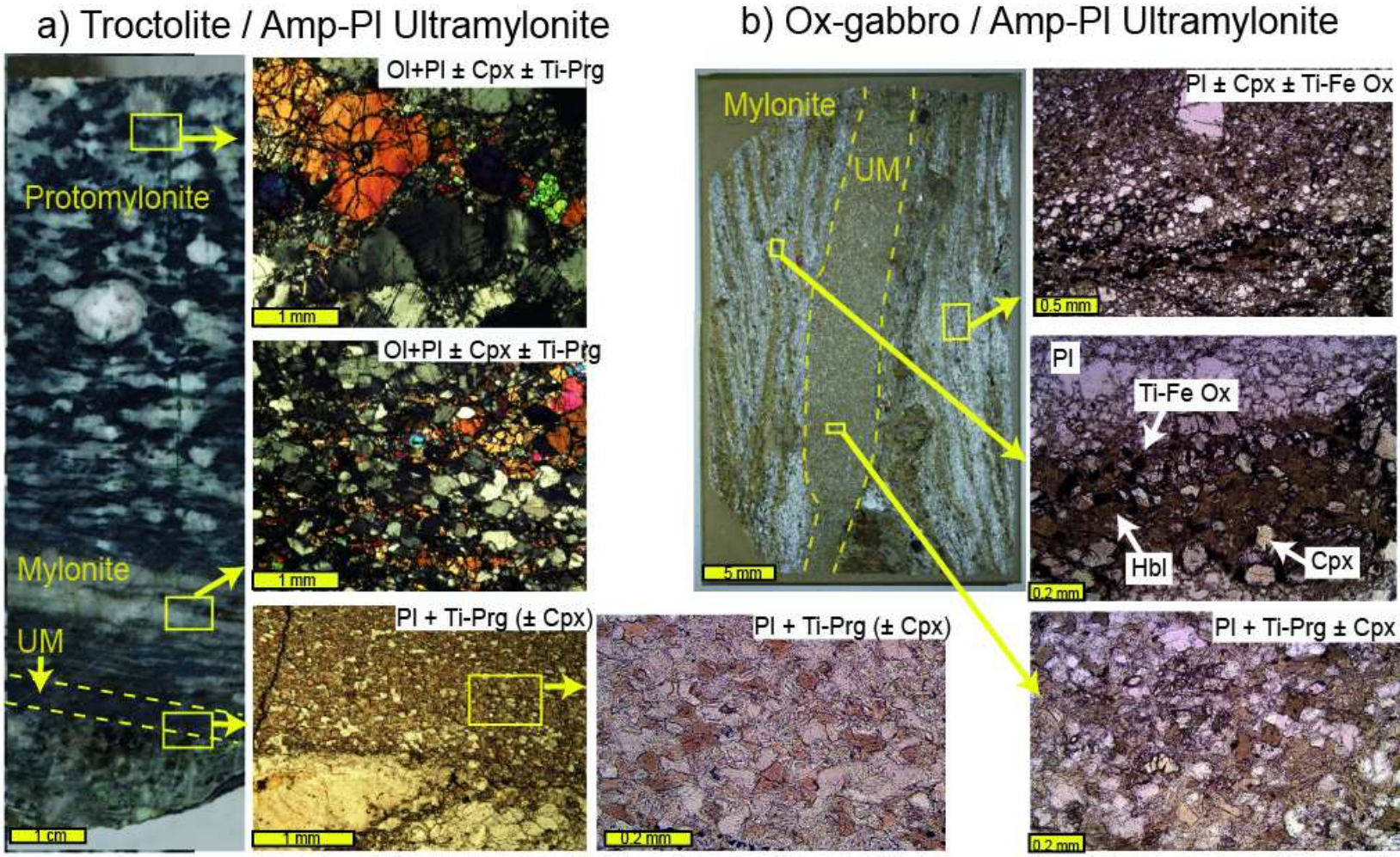
a) Troctolite / Amp-Pl Ultramylonite
b) Ox-gabbro / Amp-Pl Ultramylonite
Protomylonite
Mylonite
UM
1 cm
Ol+Pl ± Cpx ± Ti-Prg
1 mm
Ol+Pl ± Cpx ± Ti-Prg
1 mm
Pl + Ti-Prg (± Cpx)
1 mm
Mylonite
UM
5 mm
Pl ± Cpx ± Ti-Fe Ox
0.5 mm
Pl
Ti-Fe Ox
Hbl
Cpx
0.2 mm
Pl + Ti-Prg (± Cpx)
0.2 mm
Pl + Ti-Prg ± Cpx
0.2 mm

Figure 7.

a) Sheared troctolite

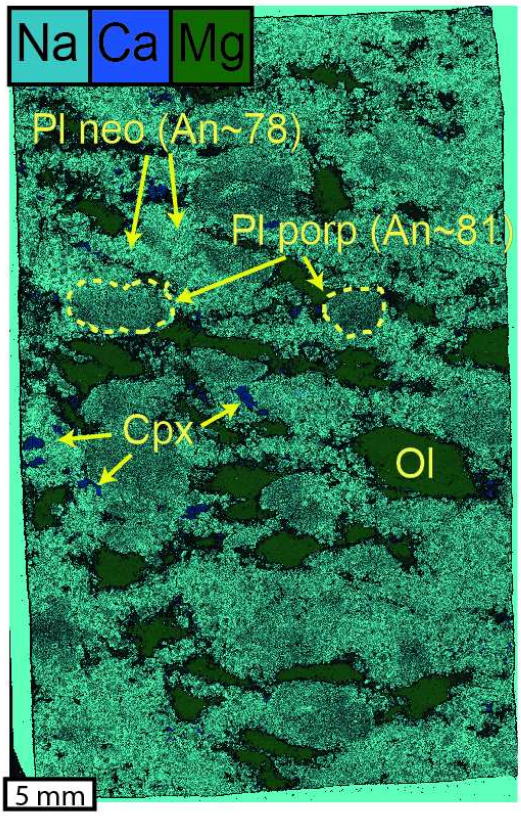

b) Troctolite / Amp-Pl Ultramylonite

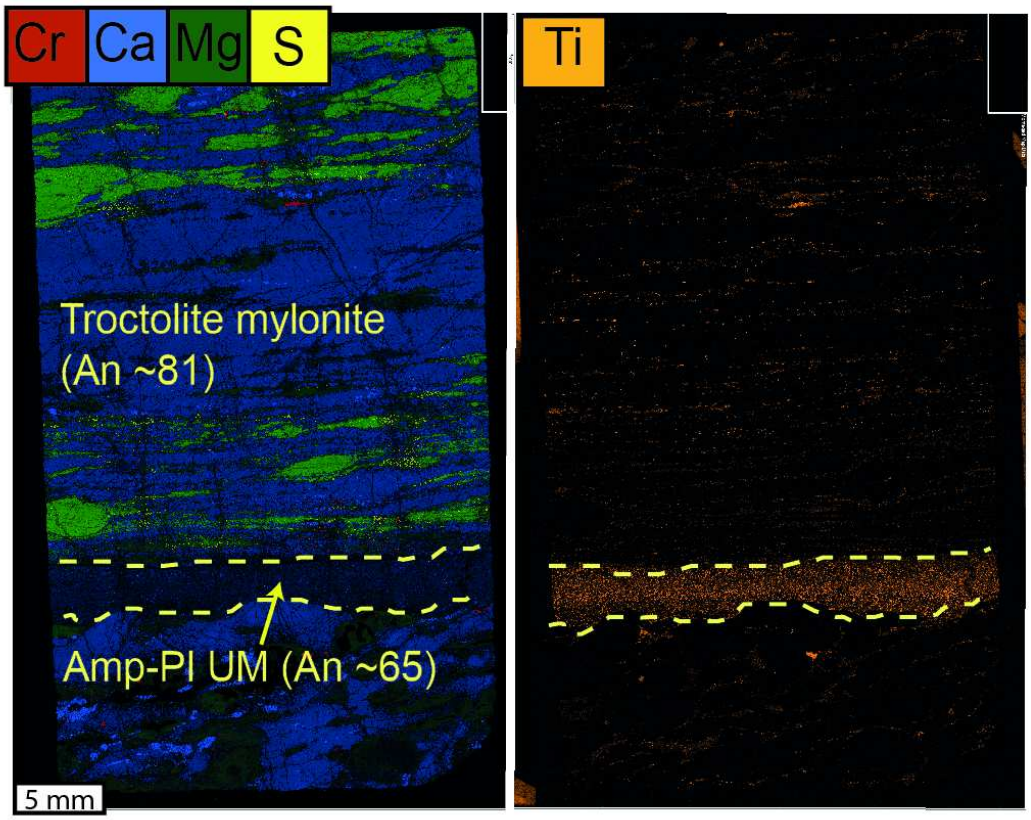

c) Ox-gabbro / Amp-Pl Ultramylonite

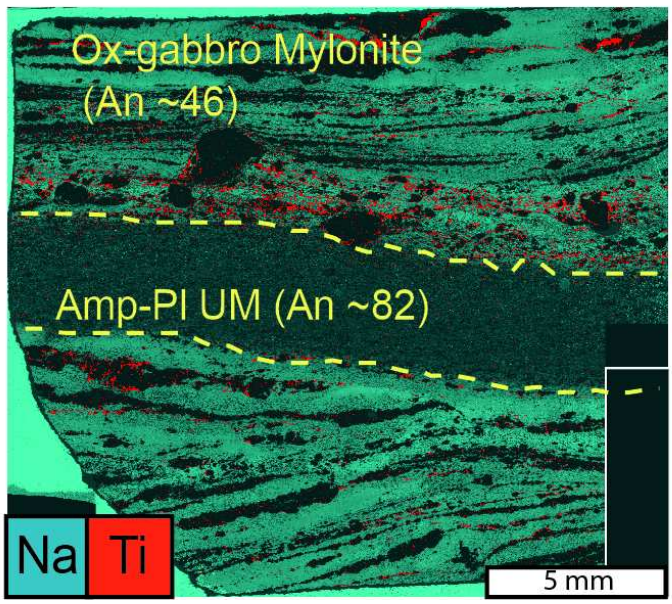

d) Amp-vein on gabbronorite

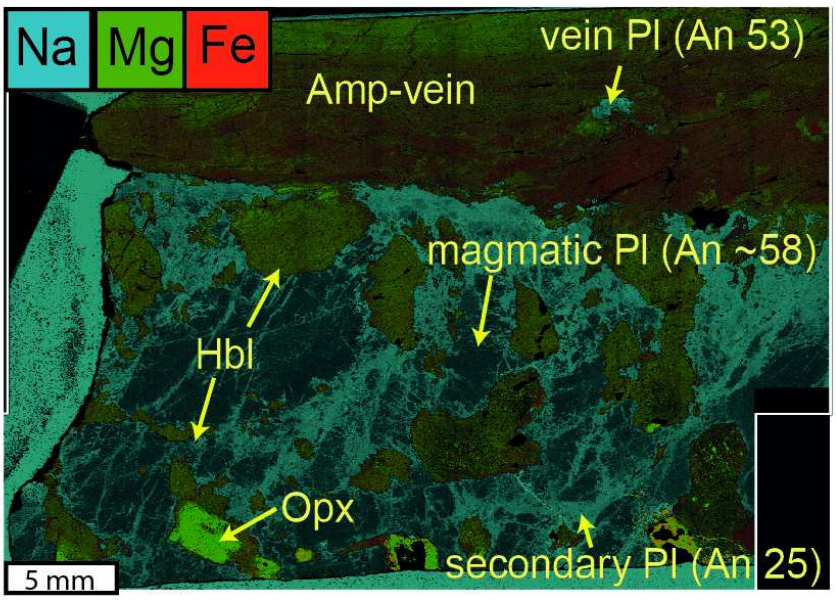

Figure 8.

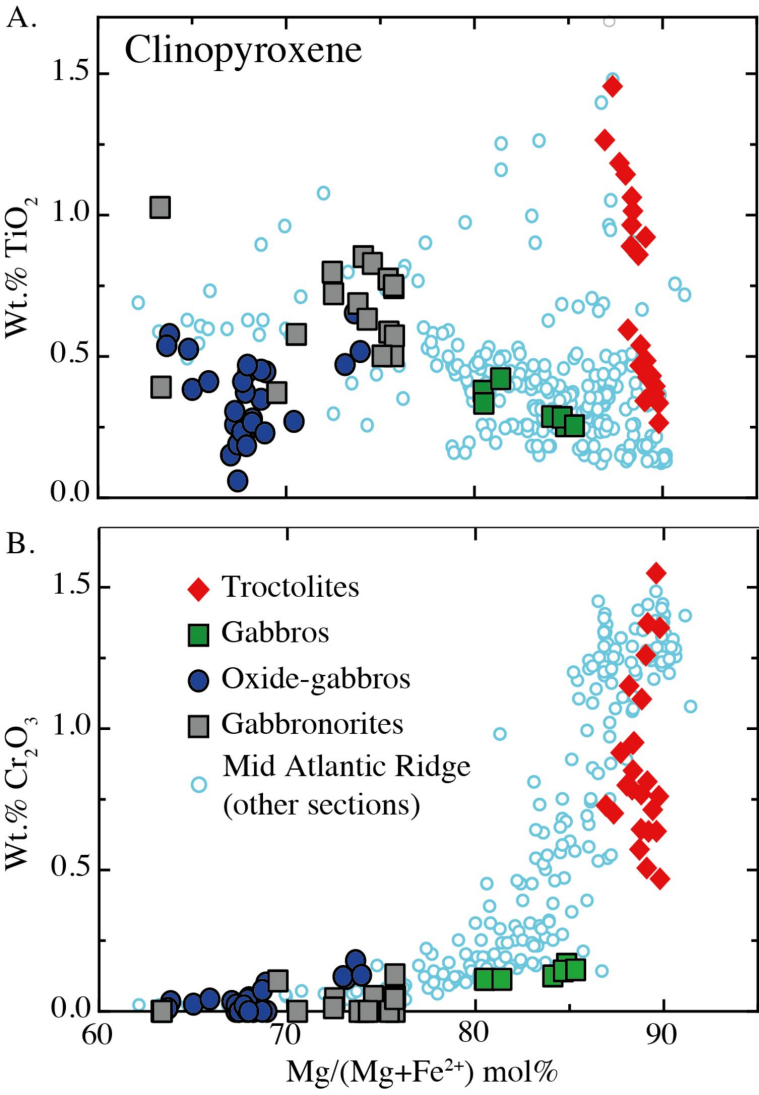
A.
Clinopyroxene
Wt.% TiO2
1.5
1.0
0.5
0.0
B.
Troctolites
Gabbros
Oxide-gabbros
Gabbronorites
Mid Atlantic Ridge
(other sections)
Wt.% Cr2O3
1.5
1.0
0.5
0.0
60
70
80
90
Mg/(Mg+Fe2+) mol%

Figure 9.

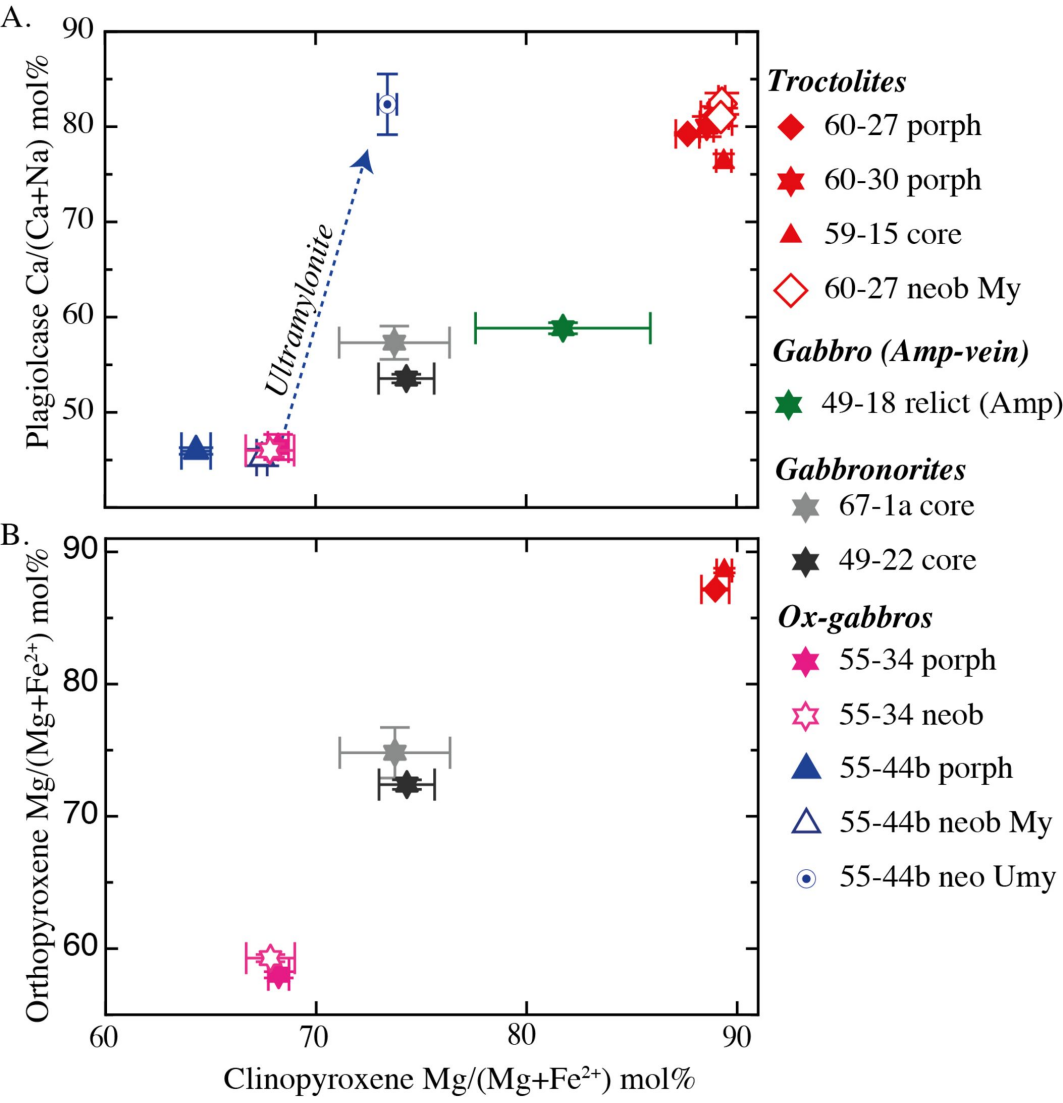
A.
B.
Plagiolcase Ca/(Ca+Na) mol%
Orthopyroxene Mg/(Mg+Fe2+) mol%
Clinopyroxene Mg/(Mg+Fe2+) mol%
90
80
70
60
50
60
70
80
90
Ultramylonite
Troctolites
60-27 porph
60-30 porph
59-15 core
60-27 neob My
Gabbro (Amp-vein)
49-18 relict (Amp)
Gabbronorites
67-1a core
49-22 core
Ox-gabbros
55-34 porph
55-34 neob
55-44b porph
55-44b neob My
55-44b neo Umy

Figure 10.

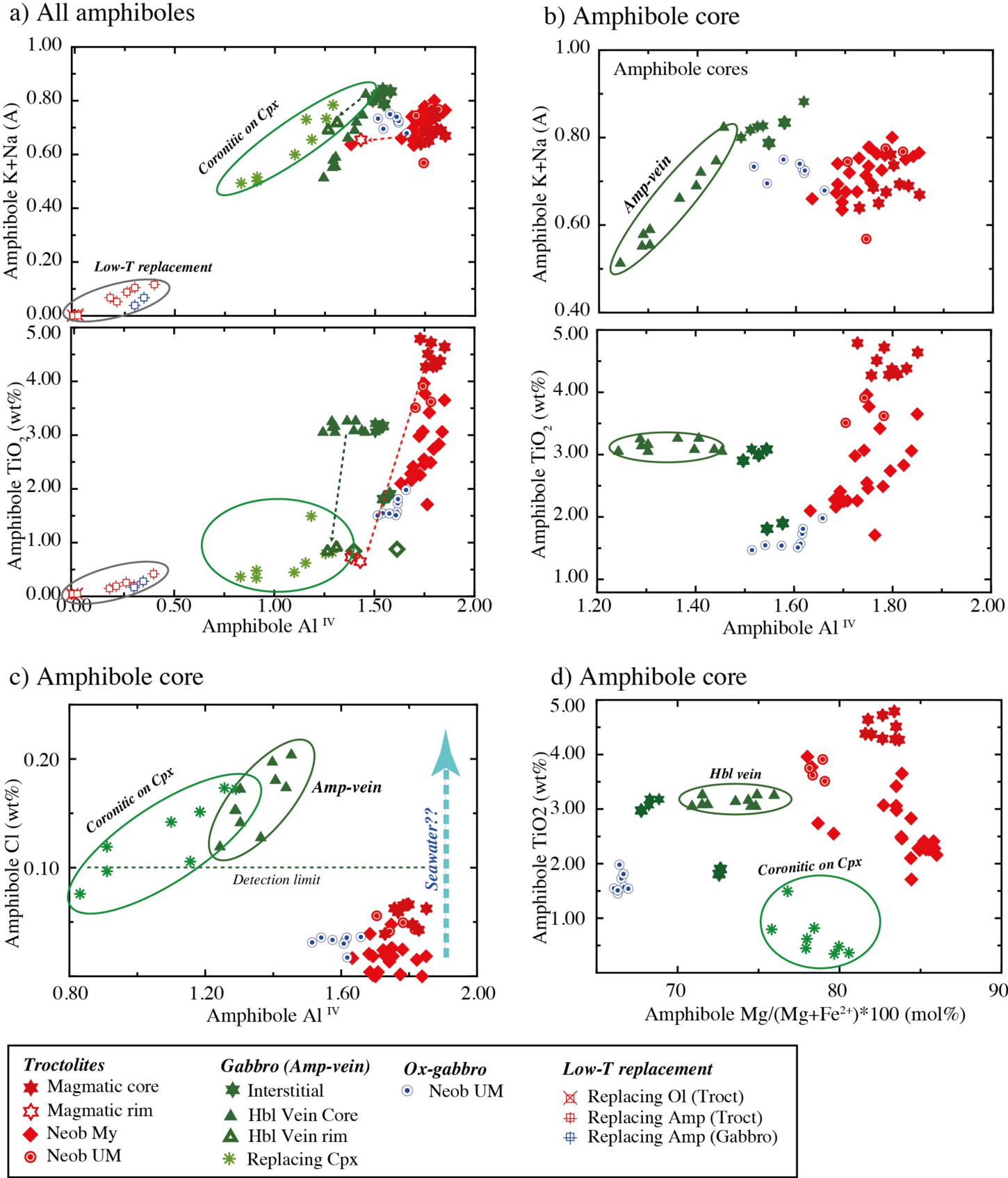
a) All amphiboles
Amphibole K+Na (A)
Coronitic on Cpx
Low-T replacement
Amphibole TiO2 (wt%)
Amphibole Al IV
b) Amphibole core
Amphibole cores
Amp-vein
c) Amphibole core
Amphibole Cl (wt%)
Coronitic on Cpx
Amp-vein
Detection limit
Seawater??
d) Amphibole core
Amphibole TiO2 (wt%)
Hbl vein
Coronitic on Cpx
Amphibole Mg/(Mg+Fe2+)*100 (mol%)
Troctolites
Magmatic core
Magmatic rim
Neob My
Neob UM
Gabbro (Amp-vein)
Interstitial
Hbl Vein Core
Hbl Vein rim
Replacing Cpx
Ox-gabbro
Neob UM
Low-T replacement
Replacing Ol (Troct)
Replacing Amp (Troct)
Replacing Amp (Gabbro)

Figure 11.

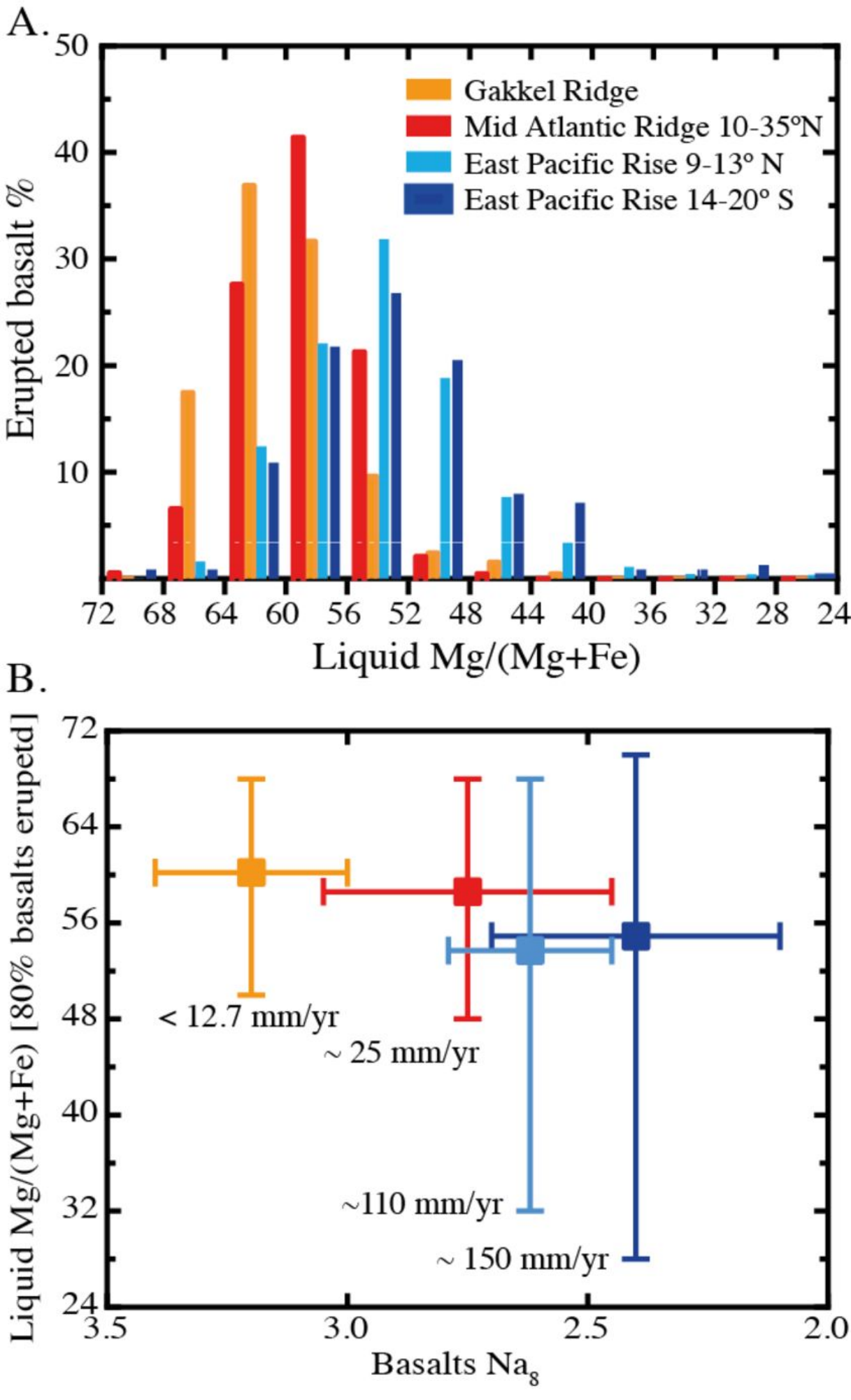
A.
Gakkel Ridge
Mid Atlantic Ridge 10-35°N
East Pacific Rise 9-13° N
East Pacific Rise 14-20° S
Erupted basalt %
50
40
30
20
10
72 68 64 60 56 52 48 44 40 36 32 28 24
Liquid Mg/(Mg+Fe)
B.
Liquid Mg/(Mg+Fe) [80% basalts erupetd]
72
64
56
48
40
32
24
< 12.7 mm/yr
~ 25 mm/yr
~110 mm/yr
~ 150 mm/yr
3.5 3.0 2.5 2.0
Basalts Na8

Figure 12.

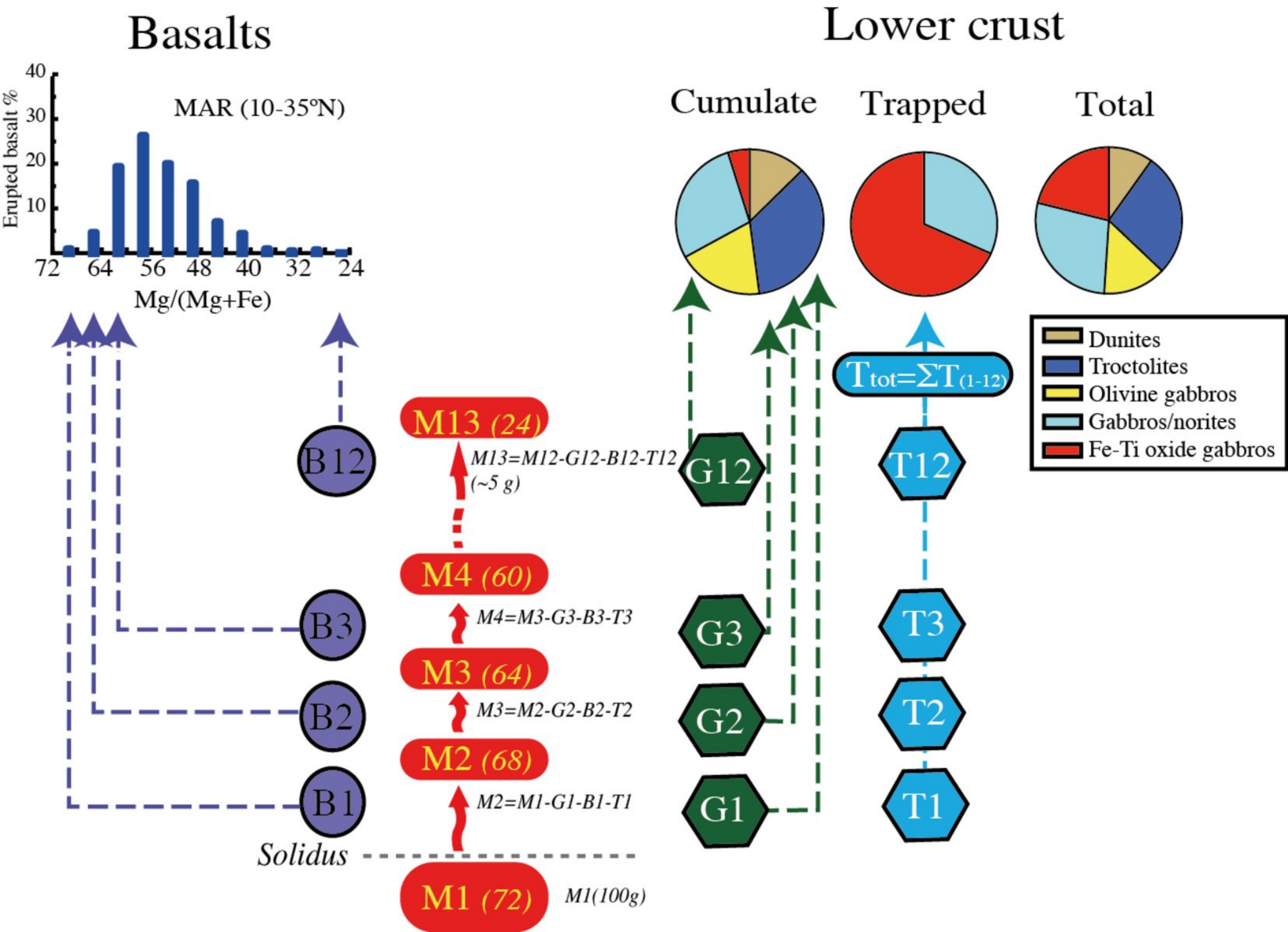
Basalts
Lower crust
Cumulate
Trapped
Total
MAR (10-35°N)
Erupted basalt %
40
30
20
10
72
64
56
48
40
32
24
Mg/(Mg+Fe)
Dunites
Troctolites
Olivine gabbros
Gabbros/norites
Fe-Ti oxide gabbros
M13 (24)
M13=M12-G12-B12-T12
(~5 g)
M4 (60)
M4=M3-G3-B3-T3
M3 (64)
M3=M2-G2-B2-T2
M2 (68)
M2=M1-G1-B1-T1
M1 (72)
M1(100g)
Solidus
B12
B3
B2
B1
G12
G3
G2
G1
T12
T3
T2
T1
Ttot=ΣT(1-12)

Figure 13.

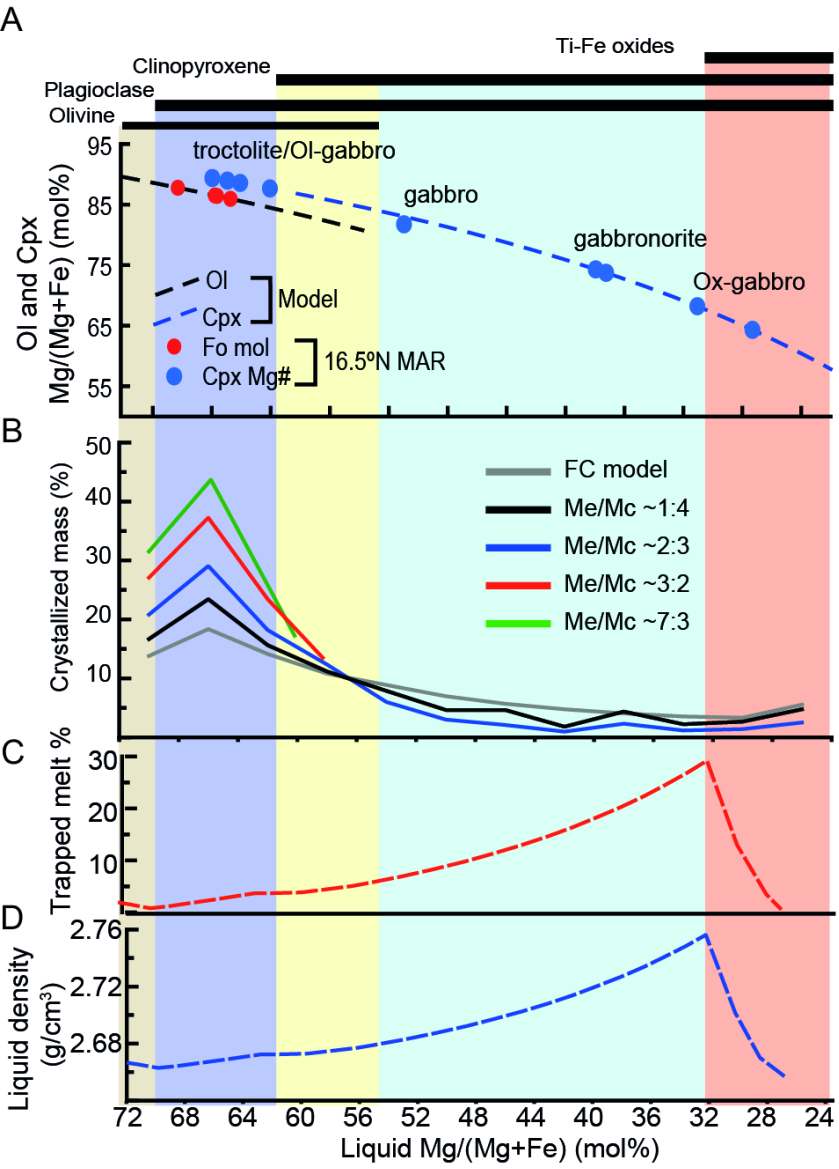
A
Clinopyroxene
Plagioclase
Olivine
Ti-Fe oxides
troctolite/Ol-gabbro
gabbro
gabbronorite
Ox-gabbro
Ol
Cpx
Model
Fo mol
Cpx Mg#
16.5ºN MAR
Ol and Cpx Mg/(Mg+Fe) (mol%)
B
FC model
Me/Mc ~1:4
Me/Mc ~2:3
Me/Mc ~3:2
Me/Mc ~7:3
Crystallized mass (%)
C
Trapped melt %
D
Liquid density (g/cm³)
Liquid Mg/(Mg+Fe) (mol%)

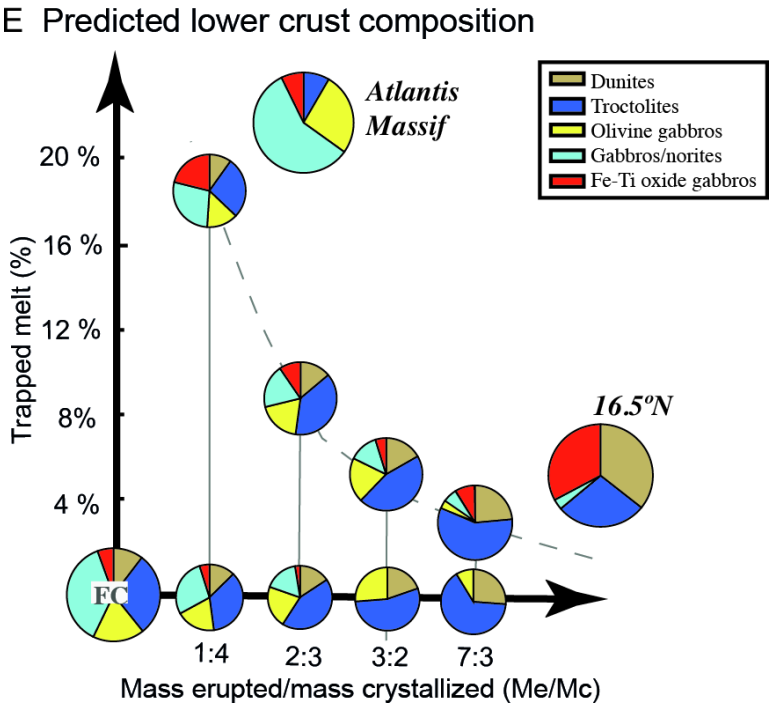
E Predicted lower crust composition
Atlantis Massif
16.5ºN
Dunites
Troctolites
Olivine gabbros
Gabbros/norites
Fe-Ti oxide gabbros
Trapped melt (%)
FC
1:4
2:3
3:2
7:3
Mass erupted/mass crystallized (Me/Mc)

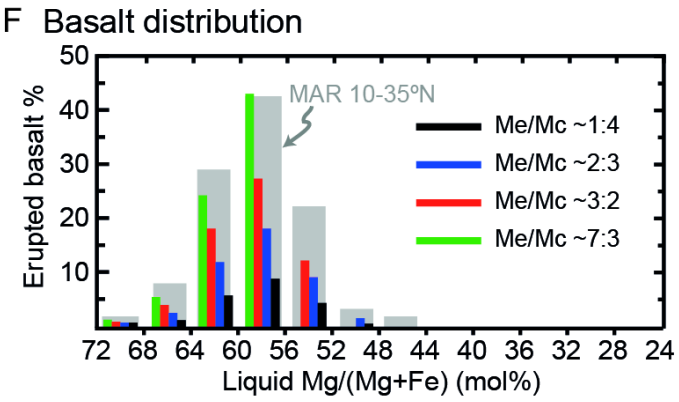
F Basalt distribution
MAR 10-35ºN
Me/Mc ~1:4
Me/Mc ~2:3
Me/Mc ~3:2
Me/Mc ~7:3
Erupted basalt %
Liquid Mg/(Mg+Fe) (mol%)

Figure 14.

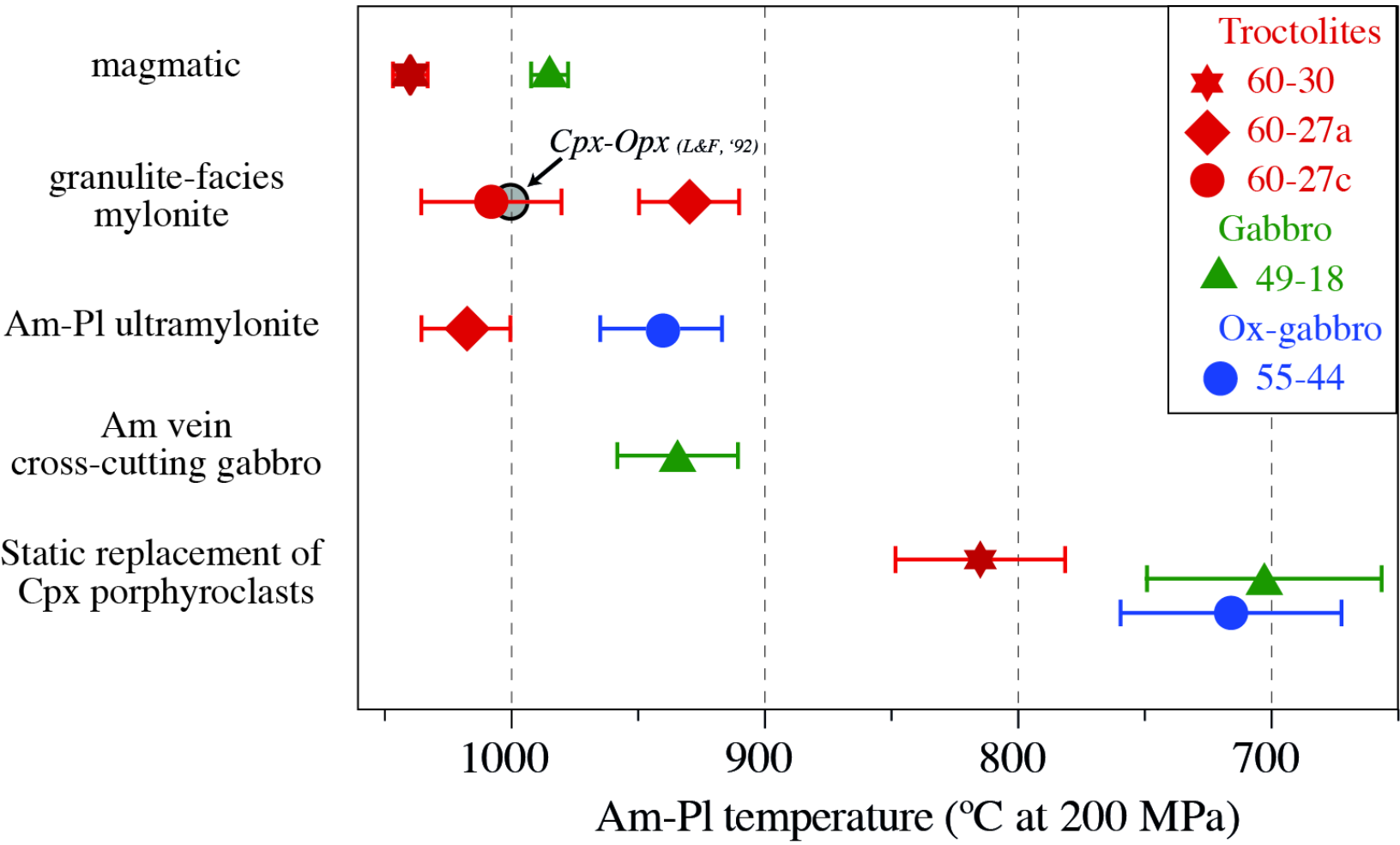
magmatic
granulite-facies mylonite
Am-Pl ultramylonite
Am vein cross-cutting gabbro
Static replacement of Cpx porphyroclasts
Cpx-Opx (L&F, '92)
Troctolites
60-30
60-27a
60-27c
Gabbro
49-18
Ox-gabbro
55-44
1000
900
800
700
Am-Pl temperature (°C at 200 MPa)